A Fully Coupled Three-Phase Model for Capillary Pressure and Relative Permeability for Implicit Compositional Reservoir Simulation

Odd Steve Hustad, SPE, Statoil, and **David John Browning,** Schlumberger

Summary

A coupled formulation for three-phase capillary pressure and relative permeability for implicit compositional reservoir simulation is presented. The formulation incorporates primary, secondary, and tertiary saturation functions. Hysteresis and miscibility are applied simultaneously to both capillary pressure and relative permeability. Two alternative three-phase capillary pressure formulations are presented: the first as described by Hustad (2002) and the second that incorporates six representative two-phase capillary pressures in a saturation-weighting scheme. Consistency is ensured for all three two-phase boundary conditions through the application of two-phase data and normalized saturations.

Simulation examples of water-alternating-gas (WAG) injection are presented for water-wet and mixed-wet saturation functions. 1D homogeneous and 2D and 3D heterogeneous examples are employed to demonstrate some model features and performance.

Introduction

The literature contains many models and correlations for modeling three-phase flow [e.g., Aziz and Settari (1979), Honarpour et al. (1986), Mattax and Dalton (1990), and Ahmed (2006)]. Many of these models employ an approach similar to that of Stone (1970, 1973), which uses saturation property dependence intended for water-wet systems. This paper focuses on the implementation of the fully coupled three-phase model described by Hustad (2002) in an implicit simulator. The formulation allows any three-phase property to be dependent on at least two two-phase properties. This approach has extended modeling flexibility and permits improved modeling capability of systems with varying wettability, without inheriting the water-wet assumptions of the more traditional models.

Experimental documentation for water-wet systems can be found in Anderson (1986, 1987a, 1987b), Oak et al. (1990), Braun and Holland (1995), and Honarpour et al. (1996). A common problem with many of these models is that they may be difficult to apply in simulations where hysteresis effects are significant or if the fluid system becomes miscible.

The Norwegian State R&D Program for Improved Oil Recovery and Reservoir Technology (SPOR) (Skjæveland and Kleppe 1992) conducted experiments of gas injection after waterflooding and complementary simulations. The modeling of the displacement experiments proved difficult (Hustad and Holt 1992). This exercise demonstrated that neither of the models from Stone was able to reproduce the experimentally observed oil recoveries. A corrective parameter was incorporated into Stone's first model (Stone 1970), enabling a match of the oil recovery for the experiment having negligible phase behavior (equilibrium gas injection). However, applying the flow parameters to the complementary experiment exhibiting significant vaporization resulted in new difficulties. It was observed that the wetting water phase was most difficult to model and that the vaporization process affected the flow behavior of the water phase.

The simulation work revealed some shortcomings in the Stone models. For example, these models do not necessarily apply the gas/oil capillary pressure at the higher gas-saturation range. That is, the gas/oil capillary pressure must be terminated at a gas saturation of one minus irreducible water saturation minus residual-oil saturation to gas at irreducible water saturation. The implication is that the maximum gas saturation modeled will be significantly lower than that measured for the gas/oil capillary pressure. This limitation can have significant implications for gas-injection projects if the modeling inherits endpoint saturations that do not permit sufficiently high gas saturation.

These limitations were the motivation for developing the model of Hustad (2002). The model described here uses the complete capillary pressure curves for all three two-phase pairs. This permits the gas saturation to achieve higher values as permitted by the crossing capillary pressure data and endpoint saturation data of Hustad and Holt (1992).

A preliminary version of the model, which was developed and tested in the RUTH program (Skjæveland et al. 1996; Hinderaker et al. 1996), showed promising results when modeling experiments with long drainage periods.

For many reservoir models, simulating with flow parameters exhibiting hysteresis is computationally intensive. The model presented here has proved to be more efficient than the earlier models and has been extended to include the modeling of miscibility (Hustad et al. 2002). The availability of a fully implicit implementation provides a more-stable solution when modeling systems exhibiting saturation-direction changes such as those inherent in hysteresis models.

Models are usually developed to study specific recovery processes for a reservoir, such as gas injection after waterflooding, WAG injection, or pressure blowdown after waterflooding. These models may be generalized to be applicable to other processes and reservoirs. When considering three-phase flow, models have usually been developed for relative permeability to oil, often assumed to be the intermediate wetting phase. This model does not have such restrictions; however, the linear dependence of the three-phase property on the two-phase properties is maintained (Oak et al. 1990). In addition, the wettability property is assumed to be incorporated in the measured two-phase data.

The model presented extends the work of Hustad (2002) by using primary saturation data in addition to hysteresis data and incorporating a number of formulation refinements. The two-phase models are first described, together with the relationship between the input and gridblock two-phase data and the primary and hysteresis saturation data, the hysteresis formulation for capillary pressure and relative permeability, and the miscibility formulation. The three-phase model is then presented, demonstrating how representative two-phase properties are used to construct the three-phase properties. WAG-injection-simulation examples are demonstrated for a selected 1D homogeneous model and 2D and 3D heterogeneous models with related capillary pressure and relative permeability curves.

Two-Phase Formulation

The formulation is constructed to ensure consistency of the three-phase properties at all two-phase boundaries. To achieve this,

process-dependent normalized saturations based on the gridblock saturations are applied to normalized input saturations, providing a direct relationship between these values.

Two-phase saturation data are entered by means of tables to allow flexibility in the characteristics of the saturation functions. The properties are made dependent on interfacial-tension (IFT) ratio or capillary-number (N_c) ratio, relating the entered saturation-function values to reference or threshold values.

The hysteresis formulation is based on two limiting scanning curves for increasing and decreasing saturations. When a saturation process experiences a change in direction, the capillary pressure is made continuous at the turning-point saturation by renormalizing the saturation range according to the endpoint and turning-point saturations, which are process-dependent. The relative permeabilities are also made continuous at the turning-point saturation by applying the same normalized saturations used for the capillary pressure.

Input. The gas/oil, gas/water, and oil/water two-phase capillary pressure and relative permeability data are entered into the simulator as functions of one of the phase pair's saturations. The data are linked to reference IFT values, which are greater than their respective threshold IFT values. The capillary pressure data are required to possess a nonzero gradient with respect to saturation. The gas/oil data are applied at zero water saturation, differing from the traditional approach.

The gas/water data are represented by the oil/water data for both the immiscible and miscible examples presented. This is done to ensure consistency for miscible runs where the hydrocarbon/water properties must be unique values of water saturation when the hydrocarbon-phase label changes at miscibility. This is especially important when using input data based on tabulated values where the oil/water and gas/water data may differ. The formulation is not restricted to using oil/water data to represent gas/water data. However, using separate gas/water data will require that the table water-saturation entries be the same and will require a scaling procedure ensuring equivalent gas/water and oil/water data at miscible conditions. This will add to the software complexity. For immiscible processes, this issue is not as important and it may not be necessary to replace the gas/water data with the oil/water data. However, the same data have been used in both the immiscible and miscible examples to facilitate comparison.

One or more sets of saturation functions may be entered, depending on the variability in properties required to model the dynamic reservoir behavior. These different sets of saturation functions are assigned to gridblocks on an appropriate regional basis. Each two-phase data set consists of three process direction

Fig. 1—Ternary representation of saturation space with two-phase relative permeability.

curves. For example, the oil/water input data are represented by a primary decreasing water-saturation curve, a secondary increasing water-saturation curve, and a tertiary decreasing water-saturation curve. The primary process always starts at 100% water saturation and/or zero gas saturation. That is, the primary process is not permitted to start at 100% oil saturation (oil/water system) or 100% gas saturation (gas/oil system). The use of three sets of curves per saturation-function set, instead of the two sets more conventionally associated with hysteresis modeling, introduces additional software complexity in terms of both data entry and data management during the simulation process. Any of the three process data sets may be equal, provided that the hysteresis- (secondary and tertiary) curve constraints described are satisfied.

The primary process data relate to the filling of the reservoir trap and are used to initialize the reservoir-simulation model. This process occurs under water-wet conditions because the reservoir is initially filled with water. As time progresses, the filled reservoir will, to some extent, change its wettability. The effect this wettability change has on the primary data is related to the reservoir's initial conditions. As the reservoir is produced, the primary process may continue to reduce the water saturation. The process may also increase and then decrease the water saturation, requiring the secondary and tertiary process data, which need not exhibit the same wettability as the primary data.

During the calculation procedure, the input saturations are normalized with respect to their endpoint saturations by

$$ S_i = \frac{\breve{S}_i - \breve{S}_{irj}}{1 - \breve{S}_{irj} - \breve{S}_{jri}}, \quad i,j = g,o,w, \quad \ldots\ldots\ldots\ldots\ldots(1) $$

relating the input values to the gridblock values. That is, the input properties are made functions of normalized saturations such that all saturation-function-table look-up is performed in normalized space of zero to unity. A more comprehensive variable description may be found in the Nomenclature.

A ternary illustration of the saturation space with the two-phase relative permeabilities and endpoint saturations is shown in **Fig. 1.** Included in this figure are three two-phase relative permeability sets of primary or secondary or tertiary data and the complementary six endpoint saturations.

Endpoint Saturations. Each gridblock is assigned six primary reference endpoint saturations and six hysteresis endpoint saturations, which, in principle, should comply with the reference IFT in the input table data. The primary and hysteresis endpoint saturations are denoted by

$$ \bar{S}_{gro}^{pr}, \bar{S}_{grw}^{pr}, \bar{S}_{org}^{pr}, \bar{S}_{orw}^{pr}, \bar{S}_{wrg}^{pr}, \text{ and } \bar{S}_{wro}^{pr} \ldots\ldots\ldots\ldots\ldots(2) $$

and

$$ \bar{S}_{gro}^{hr}, \bar{S}_{grw}^{hr}, \bar{S}_{org}^{hr}, \bar{S}_{orw}^{hr}, \bar{S}_{wrg}^{hr}, \text{ and } \bar{S}_{wro}^{hr}, \ldots\ldots\ldots\ldots\ldots(3) $$

respectively.

Because the primary process always starts at 100% water saturation and/or zero gas saturation, for consistency the primary and hysteresis endpoint saturations for S_{org}, S_{wrg}, and S_{wro} must be equal.

For gridblocks in a two-phase state, the simulation gridblock saturations are normalized as in Eq. 1, where the endpoint saturations and saturations are those pertaining to the gridblock. The gridblock reference endpoint saturations may also be made dependent on either IFT or capillary number. This invokes a scaling on the endpoint saturations as the fluid properties and flow conditions change.

The capillary number is defined as

$$ N_{cij} = \frac{u_i \mu_i}{\sigma_{ij}}. \quad \ldots\ldots\ldots\ldots\ldots\ldots\ldots\ldots\ldots\ldots\ldots\ldots\ldots(4) $$

The same endpoint-saturation scaling is also applied to the relative permeability formulation described later. The scaling requires specification of threshold values that indicate whether
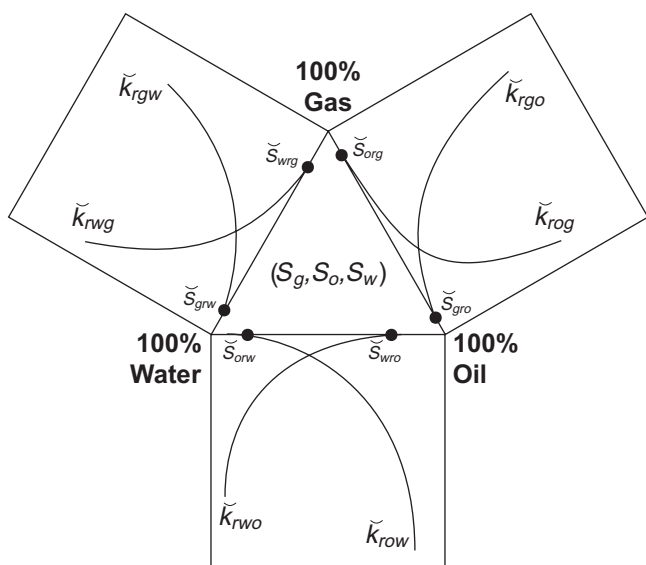
scaling should be invoked. Above the IFT threshold value, the endpoint-saturation property remains unaltered, whereas, below the threshold value, the scaling is applied.

The scaling function for IFT is

$$f_{ij}^{IFT} = \left(\frac{\sigma_{ij}}{\sigma_{ij}^{th}}\right)^{n_{ij}} \dots \dots \dots \dots \dots \dots \dots \dots \dots \dots \dots (5)$$

and for capillary number is

$$f_{ij}^{N_c} = \left(\frac{N_{cij}^{th}}{N_{cij}}\right)^{m_{ij}}, \dots \dots \dots \dots \dots \dots \dots \dots \dots \dots \dots (6)$$

where σ_{ij}^{th} and N_{cij}^{th} are the user-specified threshold IFT and capillary number, respectively, and n_{ij} and m_{ij} are user-defined constants. Six threshold capillary-number values need to be defined, whereas only three IFT threshold values are required. The gridblock endpoint saturations are then scaled as

$$\hat{S}_{irj}^{m,\kappa} = \overline{S}_{irj}^{\kappa} \cdot f_{ij}^{\eta}, \dots \dots \dots \dots \dots \dots \dots \dots \dots \dots \dots (7)$$

where κ refers to pr or hr and η refers to IFT or N_c. Similarly, for the capillary-number scaling, the capillary number must be greater than the threshold value for the scaling to be applied.

The gridblock endpoint saturations may also be process dependent, as presented by Land (1968). This is most relevant for the primary endpoint saturations that differ from the hysteresis endpoint saturations. However, the process-dependent endpoint-saturation scaling may be applied to any or all endpoint saturations. The process-dependent scaling is modeled by

$$\hat{S}_{irj}^{\kappa} = \frac{\overline{S}_i^{max}}{1 + \frac{\overline{S}_i^{max}}{\hat{S}_{irj}^{m,\kappa}} - \frac{\overline{S}_i^{max}}{1 - \hat{S}_{jri}^{m,\kappa}}}, \dots \dots \dots \dots \dots \dots (8)$$

where $i \neq j$, $\overline{S}_i^{max}$ is the maximum i-phase saturation experienced by the gridblock and

$$\overline{S}_i^{max} \leq 1 - \hat{S}_{jri}^{m,\kappa}. \dots \dots \dots \dots \dots \dots \dots \dots \dots \dots (9)$$

Switching from primary to hysteresis curves requires special treatment of the endpoint saturations to ensure smoothness in the normalized saturations during switching. The criteria for switching from primary to hysteresis curves are
• The saturation-direction change has occurred.
• The saturation is within the bounds of the hysteresis endpoint saturations.
• The relative permeability value is within the bounds of the hysteresis relative permeability.

Once the switching criteria are fulfilled and switching has occurred, the endpoint saturations will start migrating from their primary-curve endpoint-saturation values to the hysteresis endpoint-saturation values by a user-defined saturation-rate dependence, $\dot{S}$. That is,

$$\overline{S}_{irj}^{t+\Delta t} = \hat{S}_{irj}^{\kappa,t} + \dot{S} \cdot \Delta t, \dots \dots \dots \dots \dots \dots \dots \dots \dots (10a)$$

$$\overline{S}_{irj}^{t+\Delta t} < \hat{S}_{irj}^{\kappa}, \dots \dots \dots \dots \dots \dots \dots \dots \dots \dots \dots (10b)$$

and

$$\left|\overline{S}_{irj}^{t} - \overline{S}_{irj}^{t+\Delta t}\right| \leq \dot{S} \cdot \Delta t. \dots \dots \dots \dots \dots \dots \dots \dots \dots (10c)$$

The gridblock endpoint saturations used in the three-phase formulation, therefore, correspond to the input reference values following the application, first, of optional IFT or capillary-number scaling (Eq. 7); second, of optional process dependence (Eq. 8); and third, for miscible models, of constraints to ensure that the two hydrocarbon and water endpoint saturations for the two hydrocarbon/water

systems are equal at equal IFTs. The maximum permitted change in endpoint saturation over a timestep (Eq. 10) is applied after these modifications and may be used to prevent excessive changes in endpoint saturation when switching from primary to hysteresis endpoint saturations if these are significantly different.

Hysteresis. An illustration of the principle behind the hysteresis model is shown in **Fig. 2,** where the saturation scale is unnormalized. This shows the capillary pressure in the upper half and the relative permeability in the lower half of the diagram separated by the saturation axis. Drawn in solid lines are the three process curves (primary, secondary, and tertiary). The thin arrows indicate a saturation-direction change from decreasing to increasing saturation. The process illustrated consists of a decrease in saturation along the primary curve before switching to the increasing hysteresis saturation curve. To ensure continuous capillary pressure and relative permeability, the turning point saturation, S^t, at which the saturation direction changes, is recorded along with the primary-curve capillary pressure and relative permeability. The corresponding capillary pressure for the increasing saturation curve is located, and the equivalent saturation, S^e, is determined. The capillary pressure curve for the increasing-saturation process, from S^e to the maximum saturation, S^{max}, is then compressed into the saturation interval from S^t to S^{max}. This is indicated by the upper thick arrow in Fig. 2. The resulting capillary pressure is then shown in the dashed line. The relative permeability employs the same saturation points to transform the increasing relative permeability curve to the dashed relative permeability line indicated by the lower thick arrow. The transformed relative permeability curve then becomes continuous at S^t and ends at the maximum relative permeability at S^{max}.

The hysteresis formulation requires two sets of two-phase-saturation functions for each phase pair, one for increasing and another for decreasing saturations. These represent the process directions as pertaining to the three-phase saturation space. The three-phase process direction mirrors onto the two-phase saturation space. Consider an increasing-oil-saturation process in the three-phase saturation space: The two-phase mirror process for the oil/water system may be increasing for both oil and water saturations. However, the two-phase mirror process for the gas/oil system may be either increasing or decreasing saturation, depending on the saturation dependence of the function in the three-phase space. If the function is dependent on gas saturation, it may be decreasing, whereas, if it is dependent on oil saturation, it may be increasing for the mirrored gas/oil system.

The hysteresis formulation requires tracking of both (ij and ik) saturation-direction indicators to ensure continuity in capillary pressure and relative permeability when switching between the hysteresis curves. When the process direction changes, for example, from decreasing to increasing saturation, the turning-point saturation,
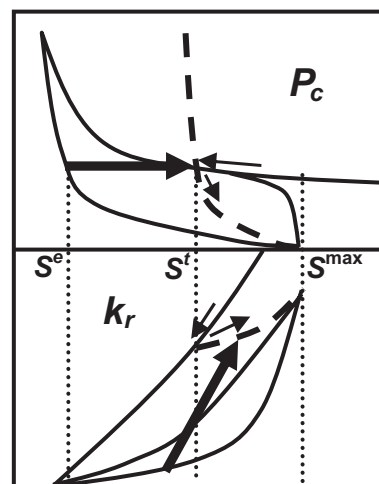

Fig. 2—Illustration of the hysteresis representation for capillary pressure and relative permeability.

S_i^t, and the equivalent saturation, S_i^e, must be determined. The turning-point saturation represents the saturation at which the process direction changes on the mirrored two-phase system. The equivalent saturation represents the saturation value for which the capillary pressure on the increasing curve equals that on the decreasing curve on the mirrored two-phase system. The input hysteresis capillary pressure curves must not cross one another. However, the input primary capillary pressure curve may cross the input hysteresis curves because the switching from primary to hysteresis occurs only once and never returns to the primary curve. The input relative permeability curves may cross one another.

Once these two saturation values have been established, the normalized hysteresis saturation is determined for the continued process with increasing saturation. The turning-point and equivalent saturations are applied as constants in the calculation of the normalized hysteresis increasing saturation:

$$S_i^h = S_i^e + \left(S_i - S_i^t\right)\left(\frac{1 - S_i^e}{1 - S_i^t}\right), S_i \geq S_i^t, \quad \dots \dots \dots \dots (11)$$

where $i = g, o, w$.

This normalized hysteresis saturation scaling has the effect of compressing the saturation range for the capillary pressure curve (increasing saturation from the equivalent saturation to unity) into the saturation range from the turning-point saturation to unity. Both the turning-point and equivalent saturations are normalized values, and they are kept fixed as long as the process direction continues in the same direction (increasing saturation).

The turning-point and equivalent saturations are recalculated when the process direction changes to decreasing saturation. For decreasing saturations, the normalized hysteresis saturation takes the form

$$S_i^h = S_i\left(\frac{S_i^e}{S_i^t}\right), S_i \leq S_i^t, i = g, o, w. \quad \dots \dots \dots \dots (12)$$

The normalized hysteresis saturation, S_i^h, is then used to look up the two-phase capillary pressure input value and allocate it to the gridblock as a representative value. The relative permeability to Phase i for a process with increasing i-phase saturation is altered slightly from Hustad (2002) in that the hysteresis loops are required to be closed at the endpoint saturations. Without this constraint, the relative permeability values may continue to drift outside the range of the two scanning curves when the process changes direction, often near the endpoint saturation.

The relative permeability to Phase i for increasing saturation is

$$\tilde{k}_{rij}(S_i) = k_{rij}^d(S_i^t) + \left[k_{rij}^i(1) - k_{rij}^d(S_i^t)\right]\left[\frac{k_{rij}^i(S_i^h) - k_{rij}^i(S_i^e)}{k_{rij}^i(1) - k_{rij}^i(S_i^e)}\right],$$
$$\dots \dots \dots \dots \dots \dots (13)$$

where k_{rij}^d and k_{rij}^i represent the input relative permeability for decreasing and increasing saturations, respectively. The hysteresis saturation, S_i^h, will start at the equivalent saturation, S_i^e, and increase to unity. The rationale behind Eq. 13 is that the first term on the right-hand side is the relative permeability value at the saturation where the process changes direction. The second term (first brackets) represents the increase in relative permeability needed to reach the maximum relative permeability on the increasing hysteresis curve. The third term (second brackets) is a term that varies from zero to unity. The increasing relative permeability values are chosen for this term to incorporate the shape of the increasing relative permeability curve. This may result in an increasing relative permeability that is fairly flat near the turning-point saturation, depending on the shape of the increasing relative permeability curve at low saturation and the amount of separation in the hysteresis curves. The curvature can be adjusted by adding a user-specified exponent to this second bracket term.

For a process with decreasing saturation, the relative permeability is

$$\tilde{k}_{rij}(S_i) = k_{rij}^d(S_i^h)\left[\frac{k_{rij}^i(S_i^t)}{k_{rij}^d(S_i^e)}\right]. \quad \dots \dots \dots \dots (14)$$

For Eq. 14, the hysteresis saturation, S_i^h, will start at the equivalent saturation, S_i^e, and decrease to zero. Eq. 13 ensures that the relative permeability will approach the limiting scanning relative permeability curve's endpoint value. Eq. 14 ensures that the relative permeability becomes zero at the normalized saturation of zero.

Each phase property is made dependent on the normalized saturation of the appropriate phase. For simulation purposes, in order to prevent excessive switching between saturation-process directions when small changes in saturation occur, a user-specified minimum saturation change must be exceeded for a change in saturation direction to occur.

Miscibility. For processes that are miscible, the capillary pressure and relative permeability are handled differently. The capillary pressure is scaled by the ratio of two IFT values. The reference IFT corresponds to the input capillary pressure and relative permeability curves. The capillary pressure scaling factor is

$$f_{ij}^{P_c} = \left(\frac{\sigma_{ij}}{\sigma_{ij}^r}\right)^{l_{ij}}, \quad \dots \dots \dots \dots \dots \dots \dots \dots (15)$$

where the exponent l_{ij} is a user-defined constant. The scaled representative capillary pressure is then

$$\hat{P}_{cij} = f_{ij}^{P_c} \cdot \tilde{P}_{cij}. \quad \dots \dots \dots \dots \dots \dots \dots (16)$$

Similarly, the representative relative permeability is scaled together with the endpoint saturations where Eq. 5 or Eq. 6 is applied:

$$\hat{k}_{rij} = \tilde{k}_{rij}, f_{ij}^\eta > 1 \quad \dots \dots \dots \dots \dots \dots \dots (17a)$$

and

$$\hat{k}_{rij} = f_{ij}^\eta \cdot \tilde{k}_{rij} + \left(1 - f_{ij}^\eta\right) \cdot S_i, f_{ij}^\eta \leq 1. \quad \dots \dots \dots (17b)$$

Eq. 17 is adopted from Coats (1980). The capillary pressure is scaled separately from the endpoint saturations and relative permeability. No bounds are placed on Eq. 15, in contrast to Eqs. 5, 6, and 17.

The two hydrocarbon and the two water endpoint saturations for the two hydrocarbon/water systems must also be equal at equal IFTs. The following equations are applied to the endpoint saturations to ensure consistency:

$$\bar{S}_{irw} = \bar{S}_{irw}^\kappa \pm \frac{1}{2}\left(1 - f_{go}^\eta\right)\left|\bar{S}_{grw}^\kappa - \bar{S}_{orw}^\kappa\right| \quad \dots \dots \dots \dots \dots (18)$$

and

$$\bar{S}_{wri} = \bar{S}_{wri}^\kappa \pm \frac{1}{2}\left(1 - f_{go}^\eta\right)\left|\bar{S}_{grw}^\kappa - \bar{S}_{orw}^\kappa\right|, \quad \dots \dots \dots \dots \dots (19)$$

where $i = g, o$. For the gas residual, "+" applies when $\bar{S}_{grw}^\kappa > \bar{S}_{orw}^\kappa$ and "−" applies when $\bar{S}_{grw}^\kappa \leq \bar{S}_{orw}^\kappa$. The same formulas are applied for the oil residual, except with opposite signs. A similar formulation may be applied to the hydrocarbon/water endpoint saturations where IFT variations are significant.

Three-Phase Formulation

The three-phase properties are based on representative two-phase properties, which are combined through a saturation-weighting scheme to obtain the three-phase properties. Each phase property is made dependent on its own normalized saturation to ensure consistency and zero relative permeability at and below the endpoint saturation. Three sets of two-phase data are applied, allowing variable endpoint saturations within the three-phase space.

On the basis of the three gridblock saturations and the six gridblock endpoint saturations, the minimum and maximum saturations

are determined for each phase. These values represent the bounds for which each phase may be mobile. The minimum and maximum saturations for Phase i are given by

$$\bar{S}_{imn} = \frac{\bar{S}_j \bar{S}_{irj} + \bar{S}_k \bar{S}_{irk} + \bar{S}_{irj} \bar{S}_{irk} \left(\bar{S}_i - 1\right)}{\bar{S}_j \left(1 - \bar{S}_{irk}\right) + \bar{S}_k \left(1 - \bar{S}_{irj}\right)} \dots\dots\dots\dots\dots(20)$$

and

$$\bar{S}_{imx} = \frac{\bar{S}_j \bar{S}_{kri} + \bar{S}_k \bar{S}_{jri} + \bar{S}_{jri} \bar{S}_{kri} \left(\bar{S}_i - 1\right)}{\bar{S}_j \bar{S}_{kri} + \bar{S}_k \bar{S}_{jri}}, \dots\dots\dots\dots(21)$$

where subscripts i, j, and k represent either the gas, oil, or water phase, and $i \neq j \neq k$.

The gridblock saturations are then normalized by

$$S_i = \frac{\bar{S}_i - \bar{S}_{imn}}{\bar{S}_{imx} - \bar{S}_{imn}}, \quad i = g, o, w. \dots\dots\dots\dots\dots(22)$$

In general, when three phases are present, the normalized saturations given by Eq. 22 do not sum to unity. However, at the two-phase boundaries, the two normalized saturations do sum to unity.

Given the normalized saturations from Eq. 22, six process-direction-dependent normalized hysteresis saturations are determined from either Eq. 11 or Eq. 12, giving two normalized hysteresis saturations associated with each of the mirrored two-phase systems. Note that the two normalized hysteresis saturations for a particular phase need not be equal for the two two-phase systems. The six process-direction-dependent normalized hysteresis saturations are represented by

$$S_g^h, S_o^h, \text{ and } S_w^h, \dots\dots\dots\dots\dots\dots(23)$$

with two for each phase. These six normalized hysteresis saturations are then applied to obtain the representative phase properties. The resulting six representative two-phase capillary pressure values are then

$$\tilde{P}_{cgo}\left(S_g^h\right), \tilde{P}_{cgo}\left(S_o^h\right), \dots\dots\dots\dots\dots(24a)$$

$$\tilde{P}_{cgw}\left(S_g^h\right), \tilde{P}_{cgw}\left(S_w^h\right), \dots\dots\dots\dots\dots(24b)$$

$$\tilde{P}_{cow}\left(S_o^h\right), \text{ and } \tilde{P}_{cow}\left(S_w^h\right), \dots\dots\dots\dots(24c)$$

and the six representative two-phase relative permeability values are

$$\tilde{k}_{rgo}\left(S_g^h\right), \tilde{k}_{rgw}\left(S_g^h\right), \dots\dots\dots\dots\dots(25a)$$

$$\tilde{k}_{rog}\left(S_o^h\right), \tilde{k}_{row}\left(S_o^h\right), \dots\dots\dots\dots\dots(25b)$$

$$\tilde{k}_{rwg}\left(S_w^h\right), \text{ and } \tilde{k}_{rwo}\left(S_w^h\right). \dots\dots\dots\dots(25c)$$

This procedure generates two representative capillary pressure values for each phase pair, which are each functions of one of the saturations in the pair. The capillary pressure, therefore, can be dependent on either of the two phases. This flexibility allows for better capillary pressure representation for three-phase conditions.

The representative capillary pressure from Eq. 24 may then be made dependent on IFT through Eq. 16. Similarly, the representative relative permeability may be made dependent on IFT or capillary number through Eq. 17.

Two alternative approaches are available for determining the capillary pressures to be used in the pressure equation. The first approach involves choosing the representative capillary pressure dependence on saturation and the weighting of these representative values in the three-phase space. This allows for ultimate user flexibility in the representation of capillary pressure for three-phase conditions and the effect of wettability. The second approach involves weighting the six representative capillary pressures by saturation, making the capillary pressure dependent on all three

saturations without requiring the user to define the dependence on saturation in the three-phase space.

First Capillary Pressure Approach. For consistency, the three capillary pressures must meet the criterion

$$P_{cgw} - P_{cgo} - P_{cow} = 0. \dots\dots\dots\dots\dots\dots(26)$$

When representative values of the capillary pressures are determined, Eq. 26 is not necessarily fulfilled using representative values and a residual R is obtained; hence,

$$\hat{P}_{cgw} - \hat{P}_{cgo} - \hat{P}_{cow} = R. \dots\dots\dots\dots\dots\dots(27)$$

To satisfy Eq. 26, the functions F, G, and H are introduced as having the property

$$F + G + H = 1. \dots\dots\dots\dots\dots\dots\dots\dots(28)$$

The representative capillary pressures may then be modified by

$$P_{cgo} = \hat{P}_{cgo} + F \cdot R, \dots\dots\dots\dots\dots\dots\dots(29)$$

$$P_{cgw} = \hat{P}_{cgw} - G \cdot R, \dots\dots\dots\dots\dots\dots\dots(30)$$

and

$$P_{cow} = \hat{P}_{cow} + H \cdot R, \dots\dots\dots\dots\dots\dots\dots(31)$$

fulfilling Eq. 26.

The functions in Eq. 28 are made dependent on saturation to meet the consistency criteria at the two-phase boundaries. The actual form of these equations in the three-phase space may depend on a number of factors, in particular, IFT, wettability, contact angles, and rock characteristics. The functional form of Hustad (2002) is employed here:

$$F = \frac{\delta_w \bar{S}_w^{\alpha_w}}{\bar{S}_w^{\alpha_w} + \left(1 - \bar{S}_w\right)^{\beta_w}}, \dots\dots\dots\dots\dots\dots(32)$$

$$H = \frac{\delta_g \bar{S}_g^{\alpha_g}}{\bar{S}_g^{\alpha_g} + \left(1 - \bar{S}_g\right)^{\beta_g}}, \dots\dots\dots\dots\dots\dots(33)$$

and

$$G = 1 - F - H. \dots\dots\dots\dots\dots\dots\dots\dots(34)$$

In addition, as an alternative to these functional forms, user-defined tables of these functions vs. saturation may also be employed for greater flexibility. These functions should fulfill the criteria

$$F\left(S_w = 0\right) = 0, F\left(S_w = 1\right) = 1, \dots\dots\dots\dots\dots(35a)$$

$$H\left(S_g = 0\right) = 0, H\left(S_g = 1\right) = 1, \dots\dots\dots\dots\dots(35b)$$

$$G\left(S_o = 0\right) = 0, \text{ and } G\left(S_o = 1\right) = 1. \dots\dots\dots\dots(35c)$$

The phase pressures are related by

$$p_o = p, \dots\dots\dots\dots\dots\dots\dots\dots\dots\dots(36a)$$

$$p_g = p + P_{cgo}, \dots\dots\dots\dots\dots\dots\dots\dots\dots(36b)$$

and

$$p_w = p - P_{cow}. \dots\dots\dots\dots\dots\dots\dots\dots\dots(36c)$$

For this first capillary pressure approach (Model 1), results are presented applying the model with the following functional dependence on capillary pressure (Eq. 24):

$$\tilde{P}_{cgo}\left(S_g^h\right), \dots\dots\dots\dots\dots\dots\dots\dots\dots (37a)$$

$$\tilde{P}_{cgw}\left(S_w^h\right), \dots\dots\dots\dots\dots\dots\dots\dots\dots (37b)$$

and

$$\tilde{P}_{cow}\left(S_w^h\right). \dots\dots\dots\dots\dots\dots\dots\dots\dots (37c)$$

Second Capillary Pressure Approach. An alternative formulation for three-phase capillary pressure is to use all six representative capillary pressures and weight these according to the gridblock saturations (Hustad 2008).

Consider the ternary diagram in **Fig. 3** for three-phase conditions with the six representative capillary pressures as depicted.

The six representative capillary pressures may be weighted as follows:

$$PCG = \frac{\overline{S}_o}{\overline{S}_o + \overline{S}_w}\hat{P}_{cgo}\left(S_g^h\right) + \frac{\overline{S}_w}{\overline{S}_o + \overline{S}_w}\hat{P}_{cgw}\left(S_g^h\right), \dots\dots\dots (38)$$

$$PCO = \frac{\overline{S}_g}{\overline{S}_g + \overline{S}_w}\hat{P}_{cgo}\left(S_o^h\right) + \frac{\overline{S}_w}{\overline{S}_g + \overline{S}_w}\hat{P}_{cow}\left(S_o^h\right), \dots\dots\dots (39)$$

and

$$PCW = \frac{\overline{S}_g}{\overline{S}_g + \overline{S}_o}\hat{P}_{cgw}\left(S_w^h\right) + \frac{\overline{S}_o}{\overline{S}_g + \overline{S}_o}\hat{P}_{cow}\left(S_w^h\right), \dots\dots\dots (40)$$

where $\overline{S}_i, i = g,o,w$ represents the gridblock saturations. Eqs. 38 through 40 can also be written, respectively, as

$$\left(\overline{S}_o + \overline{S}_w\right)PCG = \overline{S}_o\left(p_g - p_o\right) + \overline{S}_w\left(p_g - p_w\right), \dots\dots\dots (41)$$

$$\left(\overline{S}_g + \overline{S}_w\right)PCO = \overline{S}_g\left(p_g - p_o\right) + \overline{S}_w\left(p_o - p_w\right), \dots\dots\dots (42)$$

and

$$\left(\overline{S}_g + \overline{S}_o\right)PCW = \overline{S}_g\left(p_g - p_w\right) + \overline{S}_o\left(p_o - p_w\right), \dots\dots\dots (43)$$

or as

$$\begin{bmatrix} \left(\overline{S}_o + \overline{S}_w\right)PCG \\ \left(\overline{S}_g + \overline{S}_w\right)PCO \\ \left(\overline{S}_g + \overline{S}_o\right)PCW \end{bmatrix} = \begin{bmatrix} \overline{S}_o & -\overline{S}_w & 0 \\ \overline{S}_g & 0 & \overline{S}_w \\ 0 & \overline{S}_g & \overline{S}_o \end{bmatrix} \begin{bmatrix} p_g - p_o \\ p_g - p_w \\ p_o - p_w \end{bmatrix}. \dots\dots (44)$$
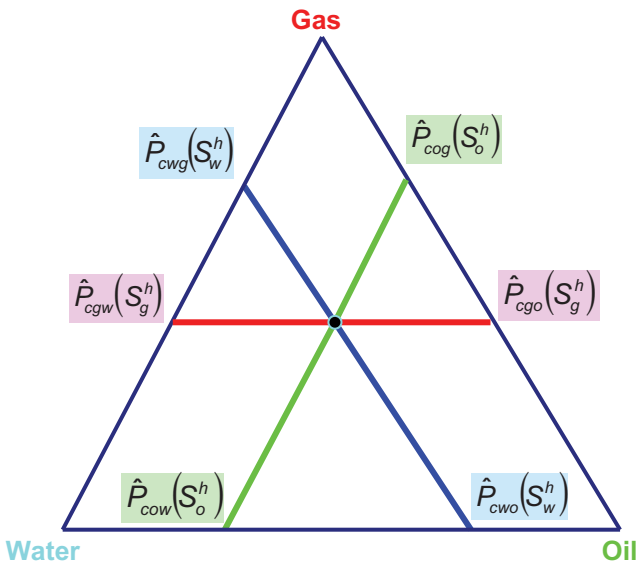
Fig. 3—Ternary diagram illustrating capillary pressure dependence on hysteresis saturation (Eq. 24).

Solving Eq. 44 for the phase pressure differences, explicit expressions are obtained in terms of the representative capillary pressures and saturations. Expressions for two-phase and single-phase boundaries may also be defined separately. Results are also presented for this second capillary pressure approach (Model 2) and, for comparison purposes, with the capillary pressures set to zero in the pressure equation (Model 0).

Relative Permeability. The three-phase relative permeabilities are determined by weighting the representative values by the gridblock saturations

$$k_{ri} = \frac{\overline{S}_j}{\overline{S}_j + \overline{S}_k}\hat{k}_{rij} + \frac{\overline{S}_k}{\overline{S}_j + \overline{S}_k}\hat{k}_{rik}, \dots\dots\dots\dots\dots (45)$$

where $i = g, o, w$ and $i \neq j \neq k$.

This formulation permits proper modeling of the two-phase mirror image of the three-phase process. Continuity is also ensured for processes changing from a three-phase state to any two-phase state.

Hydrocarbon/Water IFT

The hydrocarbon/water IFT is modeled by

$$\sigma_{iw} = A\left(\Delta\rho\right)^2 + B\Delta\rho + C, i = g,o, \dots\dots\dots\dots\dots (46)$$

where A, B, and C are user-defined constants and

$$\Delta\rho = \rho_w - \rho_i, i = g,o. \dots\dots\dots\dots\dots\dots\dots (47)$$

Note that Eq. 47 assumes the water density to be greater than the hydrocarbon density.

Implementation Considerations

Whereas the implicit pressure, explicit saturation (IMPES) implementation is comparatively straightforward, although complicated by the housekeeping requirements for the saturation-process directions and endpoint saturations, together with the equivalent and turning-point relative permeabilities and saturations, the adaptive and fully implicit implementations are substantially more complicated. The normalized saturations are each functions of three gridblock phase saturations and four associated saturation endpoints, which, in turn, are functions of IFT or capillary number and, hence, of composition. Moreover, the combination of the representative two-phase capillary pressures and relative permeabilities to generate the respective three-phase properties are subject to further weighting terms that are also functions of IFT or capillary number. Therefore, derivatives associated with each stage of the calculation process must be propagated through the calculations for the normalized saturations, the alternative saturation-process directions, and the final realization of the three-phase properties. Models tested to date have shown improved stability with the implicit implementations, as compared to IMPES, in particular when transitions from low primary to comparatively high hysteresis endpoint saturations are involved.

Examples and Discussions

The 1D example from Hustad (2002) and the 2D examples from Hustad et al. (2002) are revisited. In addition, a 3D sector model is applied. These examples demonstrate some important features of the formulation.

1D Homogeneous Example. The assumption is made that the immiscible flooding process occurs horizontally along the 1D segment of an oil column. The model parameters are listed in **Table 1.** The saturation functions are shown in **Fig. 4.** Specific details on table values are found in ECLIPSE (2009). The saturation functions are typical water-wet functions in which the functional dependence of capillary pressure on saturation uses Model 1 (Eq. 37).

The producing well is located in the last gridblock (100), the water injector is located in the second gridblock, and the gas injector

TABLE 1—DATA USED IN IMMISCIBLE 1D EXAMPLES	
Parameter	Value
Permeability (md)	500
Porosity (%)	25
Length (cm)	342
Pore volume (cm^3)	1000
Initial water volume (cm^3)	151
Initial pressure (atm)	34.753
$S_{gro}^{pr} / S_{gro}^{hr}$	0.0001/0.03
$S_{grw}^{pr} / S_{grw}^{hr}$	0.0001/0.06
$S_{org}^{pr} = S_{org}^{hr}$	0.04
$S_{orw}^{pr} / S_{orw}^{hr}$	0.0/0.2
$S_{wrg}^{pr} = S_{wrg}^{hr}$	0.05
$S_{wro}^{pr} = S_{wro}^{hr}$	0.15
Average fluid densities $g/o/w$ (g/cm^3)	0.2865/0.5196/0.9550
Average fluid viscosities $g/o/w$ (cP)	0.0364/0.1460/0.3050
Hydrocarbon-water IFT constants $A/B/C$	20/1/15
Eq. 15 IFT ratio exponents $go/gw/ow$	0.25/0.25/0.25
All exponent terms in Eqs. 5 and 18	1
Reference IFTs $go/gw/ow$ (mN/m)	17/27/27
Threshold IFTs $go/gw/ow$ (mN/m)	1.0/1.0/1.0
Rock compressibility (atm^{-1})	7.09275×10^{-5}
Water compressibility (atm^{-1})	5.06625×10^{-5}
Reservoir temperature (°C)	140

is located in the first gridblock. The production well is maintained at constant bottomhole pressure (BHP) of 342 atm, and the injection wells are maintained at constant reservoir injection rates.

The reservoir hydrocarbon composition is modeled using the Soave-Redlich-Kwong equation of state, and the model parameters and composition are those of Table 2 in Hustad and Dalen (1993).

The injection-gas mixture is the equilibrium gas composition at the bubblepoint pressure.

Commencing with water, alternating equal reservoir volumes of water and gas in cycles of 15 hours each flood the 1D segment. The reservoir rates are 10 cm^3/h. Hence, 15% of the segment's total pore volume is flooded during each injection cycle.
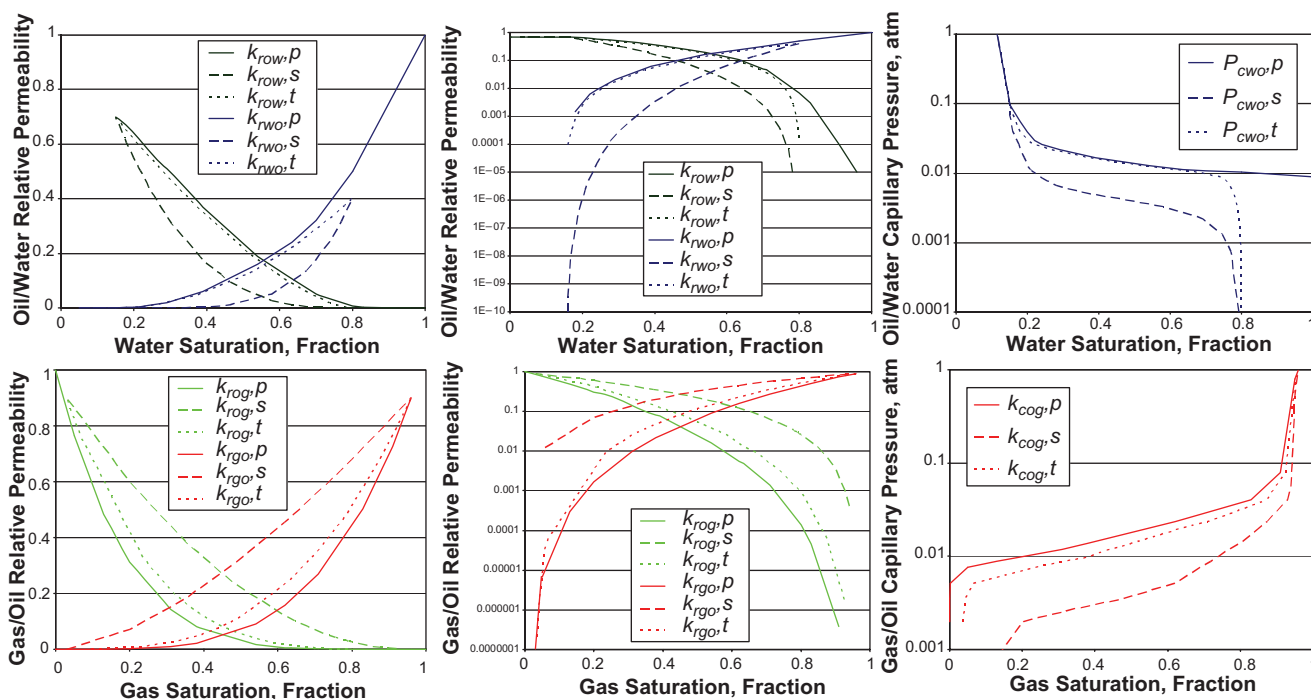
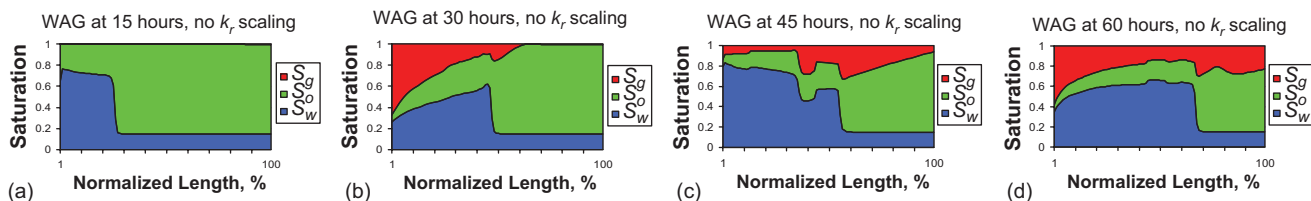Fig. 4—1D model's relative permeability and capillary pressure data; see tabulated values in ECLIPSE (2009).
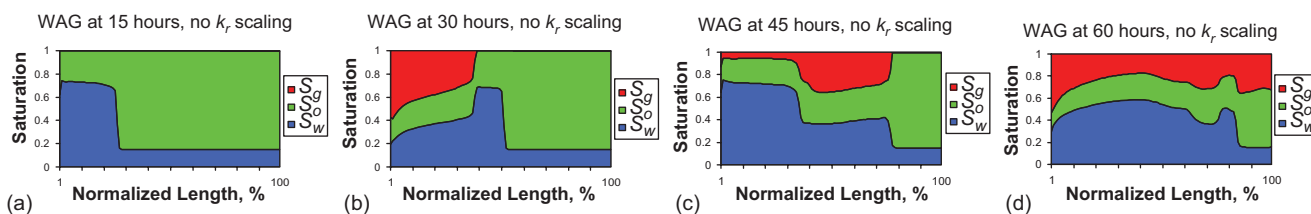
Fig. 5—Saturation profiles for 1D scenario using Model 1. Linear functions of *F* and *H*, IFT scaling on capillary pressure, and no scaling of relative permeability and endpoint saturations are applied.
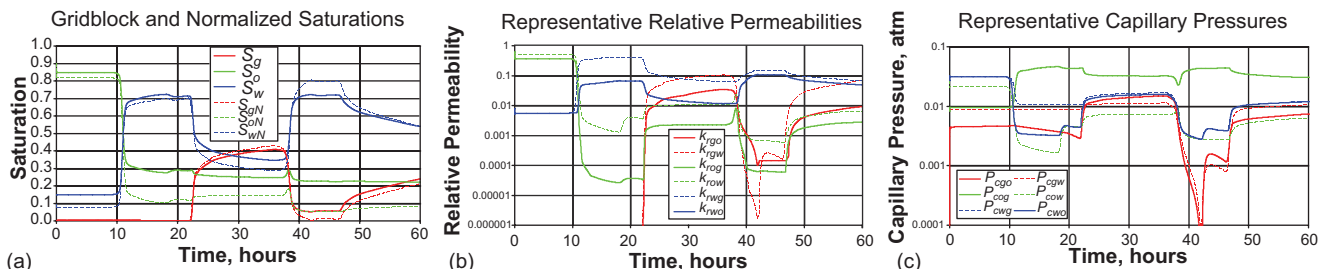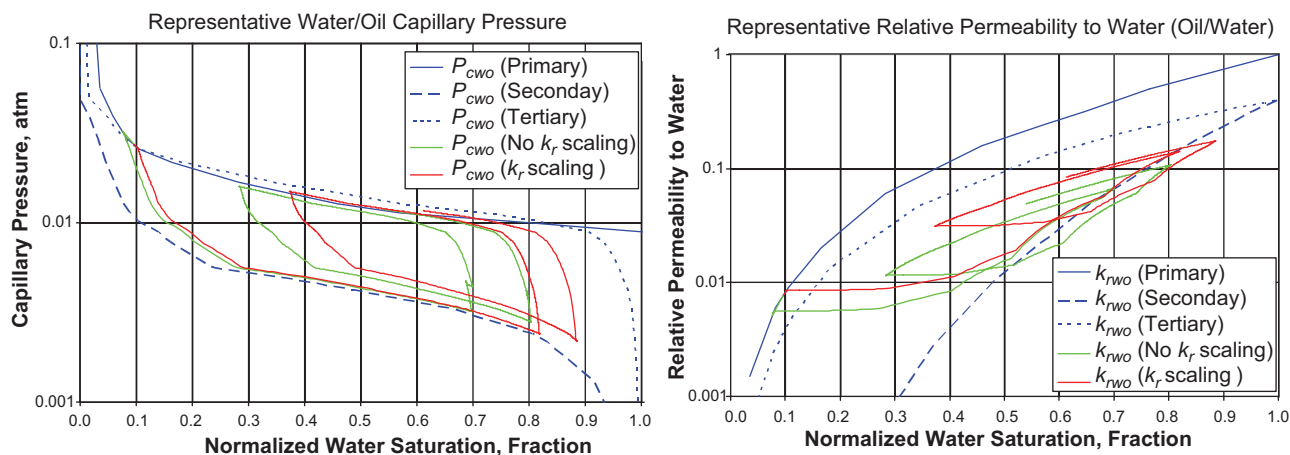

Fig. 6—Saturation, representative relative permeability, and capillary pressure development in Gridblock 20.

Fig. 5 illustrates the resulting saturation profiles for the 1D example at the end of each injection cycle for capillary pressure Model 1. These results incorporate capillary pressure scaling but no relative permeability and endpoint-saturation scaling, and minimal phase-behavior effects. A linear function is chosen for Eqs. 32 and 33 (i.e., all function parameters are set to unity).

Gridblock 20 is chosen to illustrate how selected parameters develop during the WAG injection. **Fig. 6a** illustrates the saturations and normalized saturations development in the gridblock. Notice the abrupt changes in these saturations when the phase front arrives. Figs. 6b and 6c show the representative relative permeabilities (Eq. 25) and representative capillary pressures (Eq. 24), respectively, as functions of normalized saturation before any scaling.

This example was also simulated with scaling applied to the relative permeabilities and endpoint saturations. The resulting saturation profiles at the end of each injection cycle are shown in **Fig. 7.** Comparing Figs. 5 and 7, the effect of the scaling upon the saturation distributions is evident.

The development of the representative oil/water capillary pressure (as a function of water saturation) and the representative relative permeability to water for the oil/water system is compared for the two examples in **Fig. 8** for Gridblock 20. Also illustrated in Fig. 8 are the primary, secondary, and tertiary input data. All data are plotted as functions of normalized water saturation.

Fig. 8 illustrates how the capillary pressure traces are confined within the two hysteresis-limiting curves, the secondary and

Fig. 7—Saturation profiles for 1D scenario using Model 1. Linear functions of *F* and *H*, IFT scaling on capillary pressure, relative permeability, and endpoint saturations are applied.

Fig. 8—Water/oil capillary pressure development (left) and representative relative permeability to water (oil/water system) (right) for case with and without scaling on relative permeability and endpoint saturations in Gridblock 20.

TABLE 2—DATA USED IN 2D EXAMPLES			
	Yellow Facies	Orange Facies	Set Plane
K (md)	1300	700	50
ϕ(%)	20	19	15
$S_{gro}^{pr}/S_{gro}^{hr}$	0.0/0.57	0.0/0.58	0.0/0.59
$S_{grw}^{pr}/S_{grw}^{hr}$	0.0001/0.592	0.0001/0.747	0.0001/0.638
$S_{org}^{pr}=S_{org}^{hr}$	0.03	0.04	0.05
$S_{orw}^{pr}/S_{orw}^{hr}$	0.0/0.106	0.0/0.15	0.0/0.281
$S_{wrg}^{pr}=S_{wrg}^{hr}$	0.147	0.159	0.353
$S_{wro}^{pr}=S_{wro}^{hr}$	0.147	0.159	0.353

Parameter	Value
Pore volume (cm^3)	3.827×10^6
Average initial pressure (atm)	197.39
Rock compressibility (atm^{-1})	4.053×10^{-5}
Reference IFTs go/gw/ow (mN/m)	20/22.5/22.5
Initial water volume (cm^3)	802 616
Reservoir temperature (°C)	121
Water compressibility (atm^{-1})	4.559625×10^{-4}
Threshold IFTs go/gw/ow (mN/m)	1.0/1.0/1.0
Hydrocarbon/water IFT constants $A/B/C$	20/1/25

tertiary curves. The trace for the scaled relative permeability and endpoint saturations (red line) differs from the nonscaled trace (green line). The effect of scaling is to transform the trace toward the higher water-saturation scale.

For the representative relative permeability to water, Fig. 8, the trace for both examples overshoots the secondary curve slightly. This is because of the direct use of the transformed secondary curve, Eq. 13, from low equivalent saturation to maximum water saturation. The scaling of the relative permeability and endpoint saturations in these examples increases the traced values of relative permeability to water (red line).

The nature of the capillary pressure dependence on saturation (or vice versa) for three-phase conditions is unclear. This is especially true for non-water-wet conditions. For the first capillary pressure approach, this dependence must be selected by the user. In contrast, the second capillary pressure approach incorporates all six representative capillary pressures in the saturation-weighting scheme, making it unnecessary for the user to specify the capillary pressure dependence on saturation for three-phase conditions. For these examples, the second capillary pressure approach showed saturation profiles similar to those of the first capillary pressure approach.

2D Cross-Sectional Example. This example is taken from Hustad et al. (2002). The model parameters are listed in **Table 2.** The cross-section model is shown in **Fig. 9.** It has a length of 5.1 m, a depth of 1 m, a height of 4.05 m, and grid dimensions of 51×1×81 (N_x, N_y, N_z). Also shown in Fig. 9 are the initial oil and water saturations at immiscible conditions, with the saturation scales depicted in **Fig. 10.** These saturation scales also apply to the following figures illustrating the saturation distributions. Three different permeability properties are distributed among the gridblocks in a crossbedding setting. **Fig. 11** shows the three sets of reference relative permeability and capillary pressure curves.

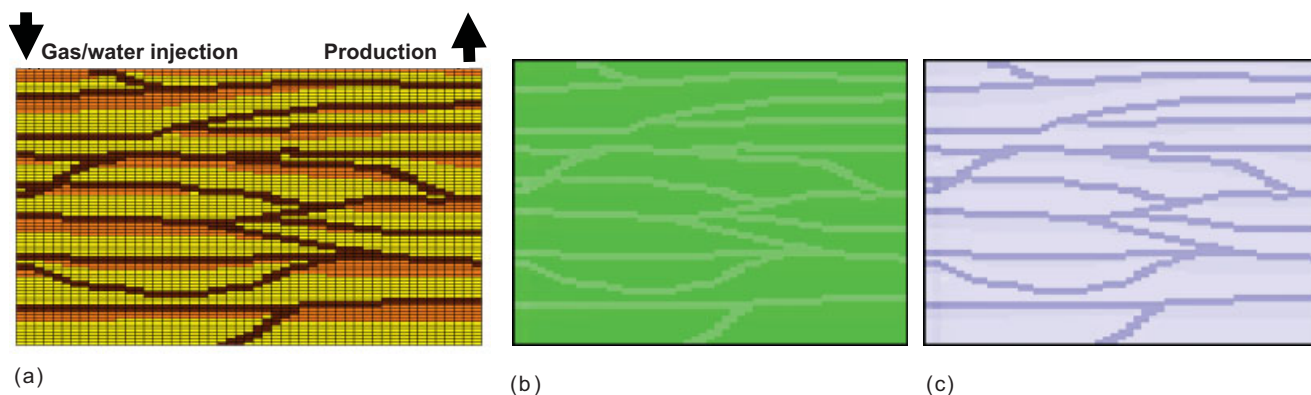(a) Gas/water injection Production

(b)

(c)

Fig. 9—(a) Simulation grid showing 2D model's permeability (lithofacies) distributions: yellow, 1300 md; orange, 700 md; brown, 50 md; initial oil (b) and water (c) saturations for immiscible example.
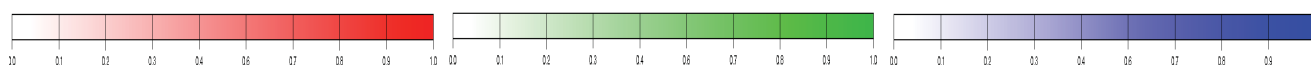

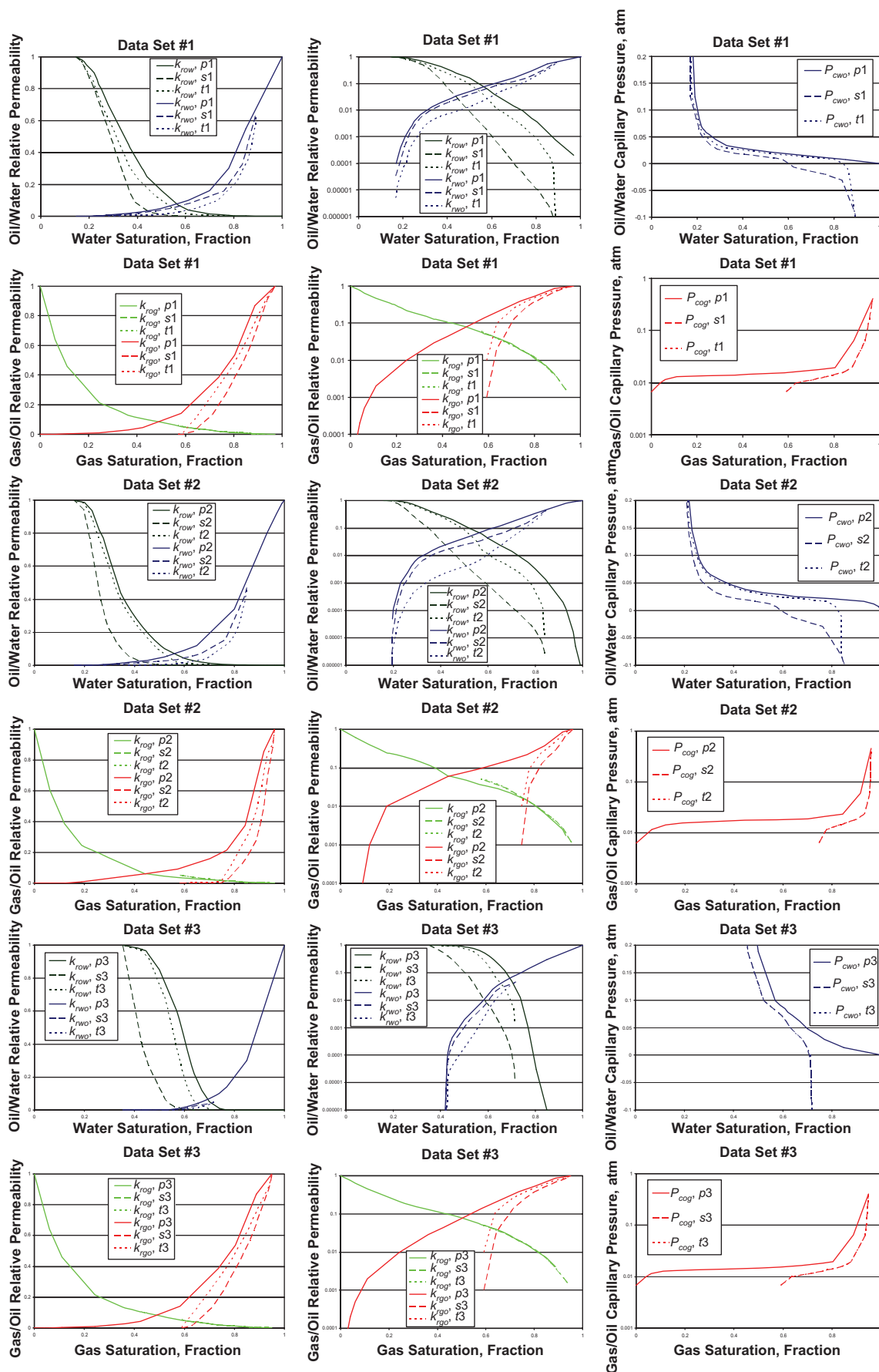Fig. 10—Gas-, oil-, and water-saturation scale legends for Figs. 12 through 18 and Figs. 21 through 23.

Fig. 11—Reference relative permeability and capillary pressure data used in the 2D model. Data Sets 1, 2, and 3 refer to yellow facies, orange facies, and set planes, respectively.
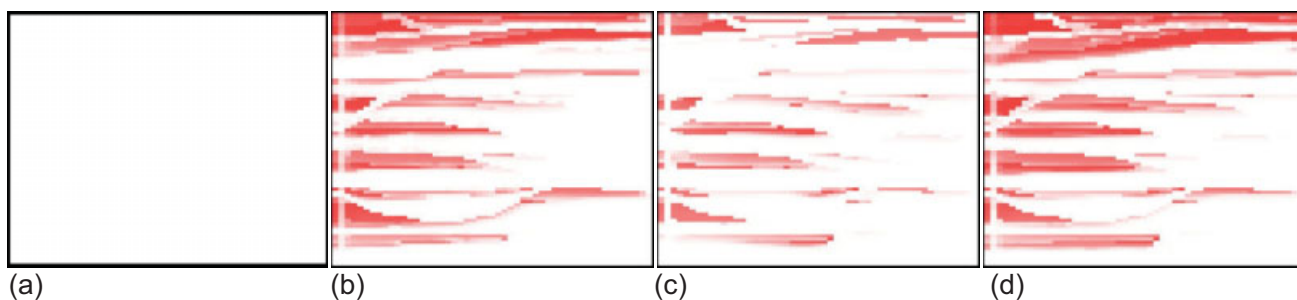
Fig. 12—Gas-saturation profiles at the end of first water-, first gas-, second water-, and second gas-injection cycles, immiscible 2D heterogeneous scenario.
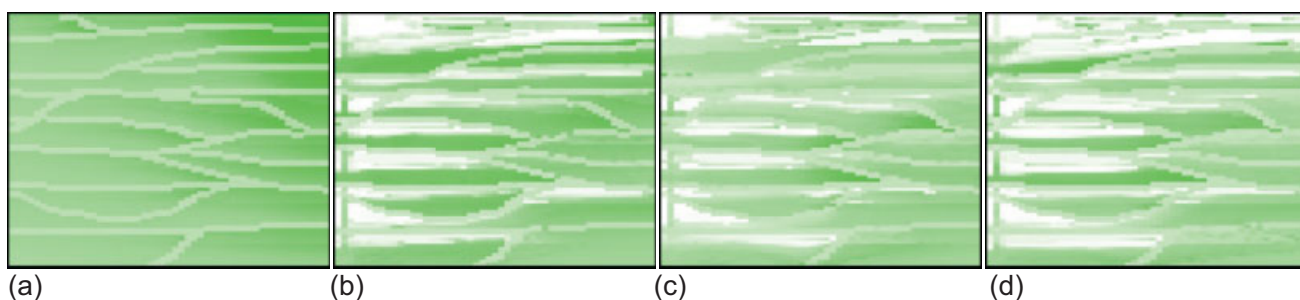

Fig. 13—Oil-saturation profiles at the end of each of the four injection cycles, immiscible heterogeneous scenario.

A WAG-injection process is simulated with four injection cycles each of equal duration (480 hours), starting with water followed by gas, then water, and ending with a gas cycle. The immiscible run injects at a constant subsurface rate of 2500 cm³/h and produces at a constant BHP of 184.533 atm, corresponding to the bubblepoint pressure. The injection gas consists of a dry-gas composition; see Table 3 of Hustad et al. (2002). The capillary pressure/saturation relationship defined by Model 1 is employed. Tabulated values of functions F and H (Eqs. 32 and 33, respectively) are applied where the functions are zero up to $S_i = 1 - S_{ori}$, $i = g, w$. This has the consequence that R in Eqs. 29 and 31 is zero throughout the simulation.

Figs. 12, 13, and 14 show the gas-, oil-, and water-saturation distributions, respectively, for the immiscible WAG-injection scenario at the end of each of the four injection cycles. The gas fingers into the high-permeability regions during gas injection but is not displaced completely during the following water-injection cycle.

The oil is displaced efficiently by the underriding first water cycle. Higher oil saturations remain in the high-permeability regions because of blockage by the low-permeability set planes. The first gas cycle reduces the oil saturation further in the high-permeability regions but simultaneously redistributes the oil, forming pools of high oil saturation in certain areas underlying the high-gas-saturation areas. This process repeats itself for each cycle pair, and the oil saturation is reduced with time.

The water profiles show that water prefers to flow where the water saturation is highest and where the resistance is least. Poorer

sweeping by water, therefore, may be observed in regions where the gas saturation is high (see Figs. 12c and 14c).

This scenario was also simulated at miscible conditions. The producing BHP was raised to 493.462 atm to obtain first-contact miscibility. **Figs. 15, 16, and 17** show the gas, oil, and water saturations, respectively, at the end of the four injection cycles.

In contrast to the immiscible WAG injection, the miscible WAG-injection scenario has significantly more gas override (see Figs. 15b and 15d). The set planes here do not act as barriers to gas flow. The oil saturation is also reduced for each injection cycle, and gas occupies more of the pore volume with each gas-injection cycle. Water, as in the immiscible WAG-injection scenario, prefers to flow along the path of least resistance, showing some water override as in the immiscible scenario (see Figs. 17c and 14c). The water is more evenly distributed vertically in the miscible scenario.

The immiscible and miscible scenarios were also simulated with a homogeneous model. The properties of the orange facies from the heterogeneous model were applied to all gridblocks in these two scenarios. Illustrated in **Fig. 18** are the gas and oil saturations at the end of the second gas cycle. Figs. 18a and 18c are from the immiscible scenario, and Figs. 18b and 18d are from the miscible scenario. The figures are an illustration of how the homogeneous model contributes to a greater gravity-override effect. Notice also that the saturations have different distributions and gas/oil contact angles because of the phase-property influence on the flow parameters relative permeability and capillary pressure.
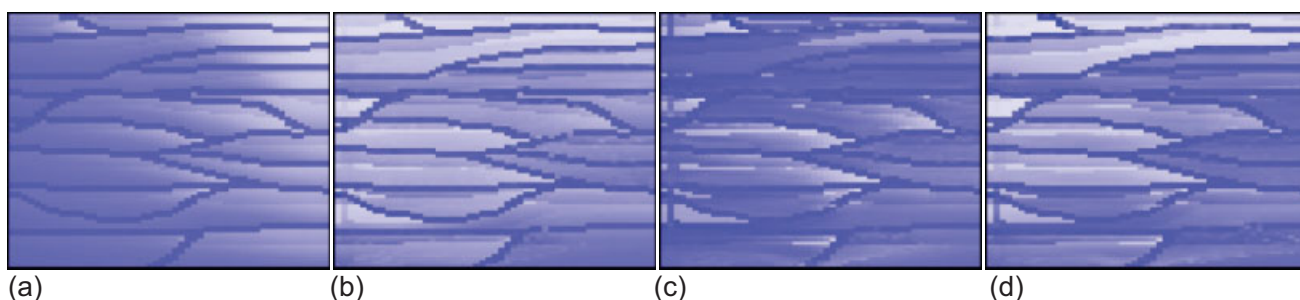

Fig. 14—Water-saturation profiles at the end of each of the four injection cycles, immiscible heterogeneous scenario.
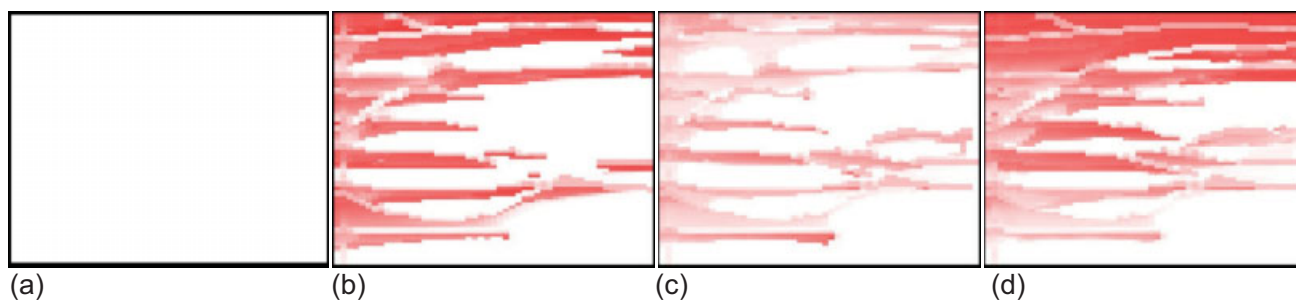
Fig. 15—Gas-saturation profiles at the end of the four injection cycles, miscible 2D heterogeneous scenario.
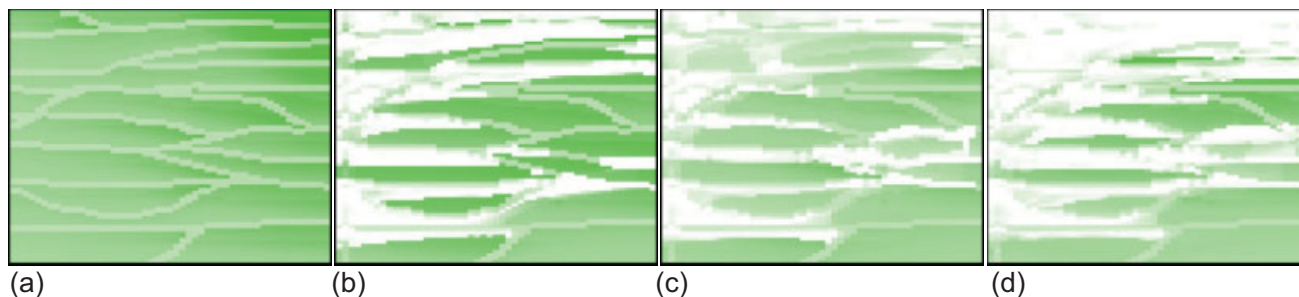

Fig. 16—Oil-saturation profiles at the end of the four injection cycles, miscible heterogeneous scenario.
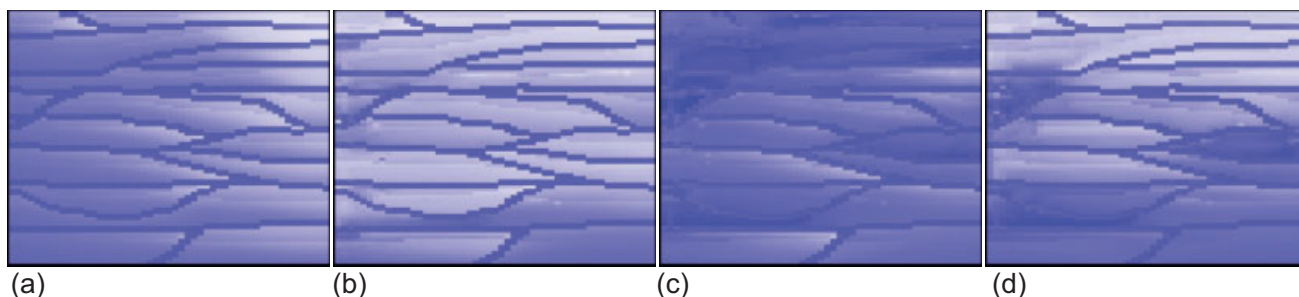

Fig. 17—Water-saturation profiles at the end of the four injection cycles, miscible heterogeneous scenario.

Fig. 19 illustrates the cumulative recoveries with time for four Model 1 scenarios. The four scenarios consist of heterogeneous and homogeneous examples run at immiscible and miscible WAG-injection conditions. The raised initial reservoir pressure for the heterogeneous miscible scenario increases the initial in-place oil volumes by 131 966 cm³, or 6.2%, in comparison with the immiscible scenario. Despite this difference in initial volumes, the oil-recovery factor of 72.5% for the miscible scenario is significantly higher compared with the immiscible-scenario recovery factor of 61.1%, as Fig. 19 shows. The immiscible homogeneous scenario produces higher oil volumes compared with the immiscible heterogeneous scenario. The miscible heterogeneous scenario results in the highest oil production of all four scenarios.

Last, Model 1 can be compared to Model 0, where the capillary pressure is zero in the pressure equation, and to Model 2, where the representative capillary pressures are weighted by saturations. The examples for Models 0 and 2 are run at immiscible WAG injection with the heterogeneous example. **Fig. 20** shows the cumulative gas, oil, and water production with time from Models 0, 1, and 2. When capillary pressure is omitted from the pressure equation (Model 0), it results in higher gas and oil production and the lowest water production. The capillary pressure dependence on a single saturation (Model 1) or multiple saturations (Model 2) results in similar water production, but Model 2 has the lower oil recovery. **Figs. 21, 22, and 23** show the gas, oil, and water saturations, respectively, for Models 0 and 2 at the end of the second water- and second
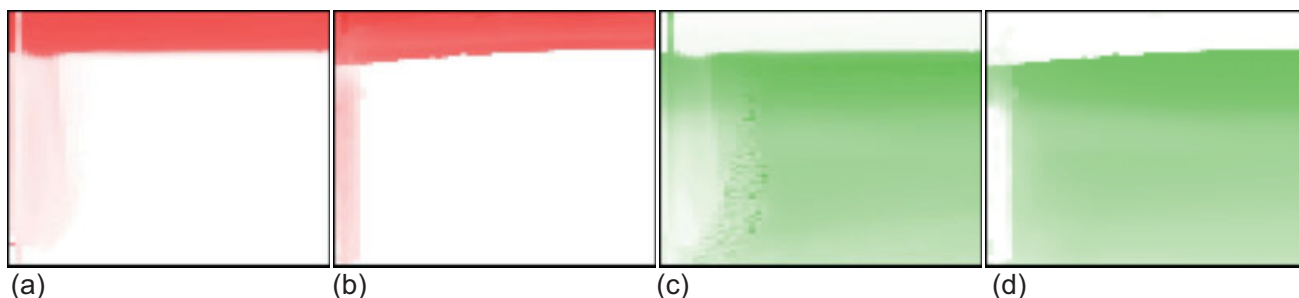

Fig. 18—Gas- (a and b) and oil- (c and d) saturation profiles at the end of the second gas-injection cycle, immiscible (a and c) and miscible (b and d) for 2D homogeneous scenarios.
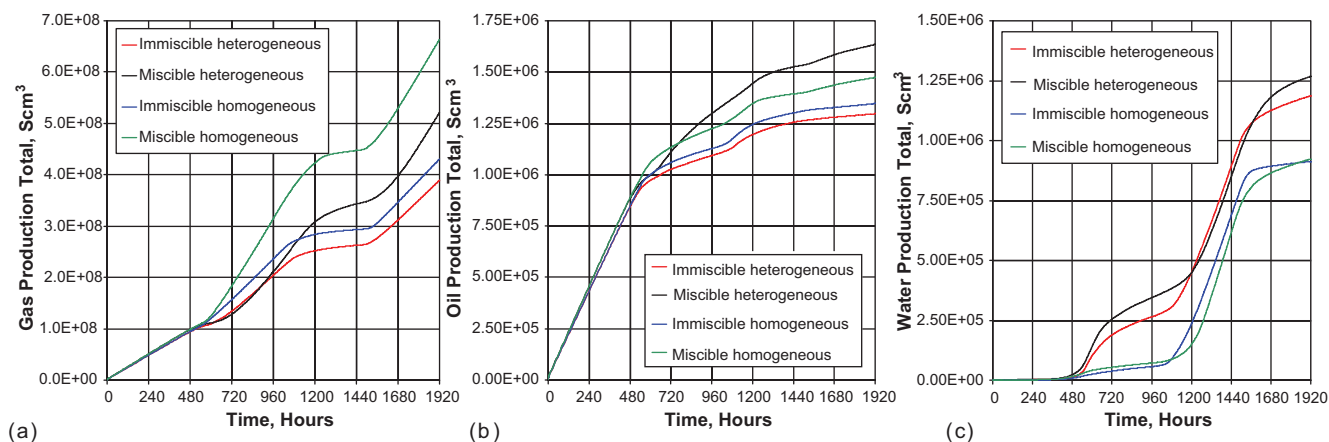
Fig. 19—Gas, oil, and water cumulative recoveries vs. time, 2D heterogeneous and homogeneous models under immiscible and miscible conditions.
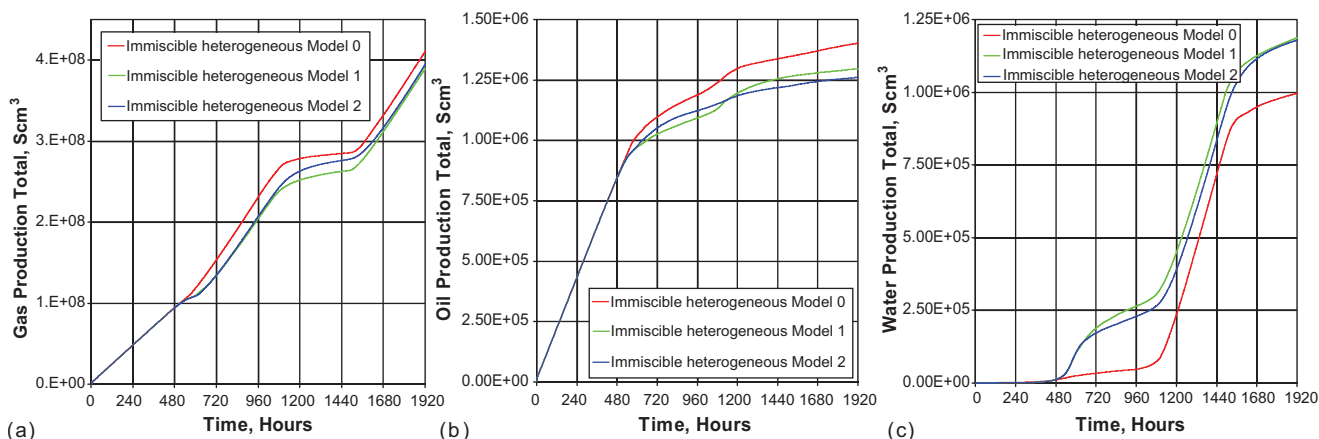

Fig. 20—Gas, oil, and water cumulative production (red, green, and blue denote Models 0, 1, and 2, respectively).

gas-injection cycles. The run with the capillary pressure being zero (Model 0) results in a stronger gas override (Figs. 21a and 21b) and water underride (not shown). Capillary pressure dependence on a single saturation (Figs. 12, 13, and 14) results in sharper and larger gas-and-water-saturation contrasts and an oil saturation that is more evenly distributed compared with capillary pressure dependence on all three saturations (Model 2, Figs. 21c, 21d, 22c, 22d, 23c, and 23d), which results in more smeared gas and water saturations and an oil saturation that is more distributed in regions of high oil saturation. Model 2 also creates more pools of high oil saturation (Fig. 22d) compared with Model 1 (Fig. 13d) and Model 0 (Fig. 22b).

Comparing the computational requirement of the three models, Models 0 and 2 used 15.5 and 115% of Model 1 usage, respectively.

3D Sector Model Example. A 3D sector model has been selected to illustrate the performance of the three-phase model. The model consists of a 27×61×32 (N_x, N_y, N_z) grid, in which a total of 10,148 gridblocks are active.

The model contains 10 different saturation function sets, where one is depicted in **Fig. 24.** Two issues may be pointed out in this figure. First, the primary relative permeability to gas crosses the hysteresis loop, and, second, the oil/water primary capillary pressure crosses the hysteresis capillary pressure.

Crossing hysteresis relative permeability curves have also been reported by others [see Spiteri et al. (2008)]. For the examples demonstrated here, no emphasis has been given to whether the secondary curves lie above or below or how they cross the tertiary curve. However, this distinction may be important for the outcome of an improved-oil-recovery study. Note also that the curves applied in these examples do not comply with those of Spiteri et al. (2008).

Fig. 25a shows a top view of the initial saturation in the model. No gas is present initially. A water-injection scenario over 4 years
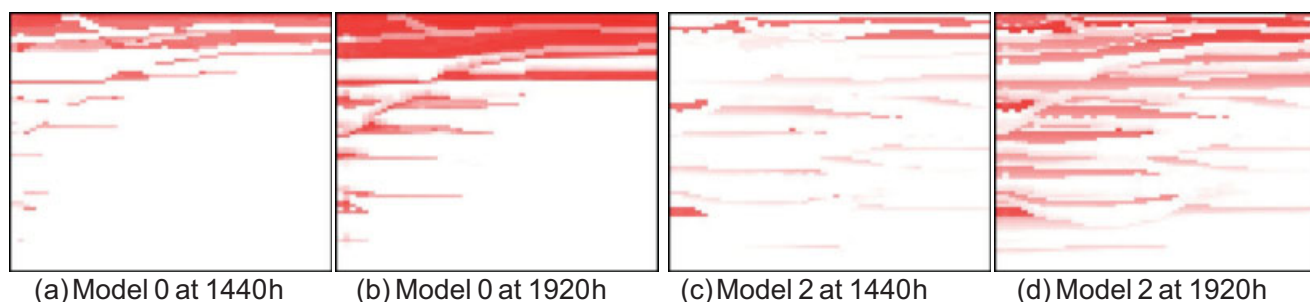

(a) Model 0 at 1440h   (b) Model 0 at 1920h   (c) Model 2 at 1440h   (d) Model 2 at 1920h

Fig. 21—Gas saturation from Models 0 and 2 after second water- and second gas-injection cycles.

(a) Model 0 at 1440h   (b) Model 0 at 1920h   (c) Model 2 at 1440h   (d) Model 2 at 1920h
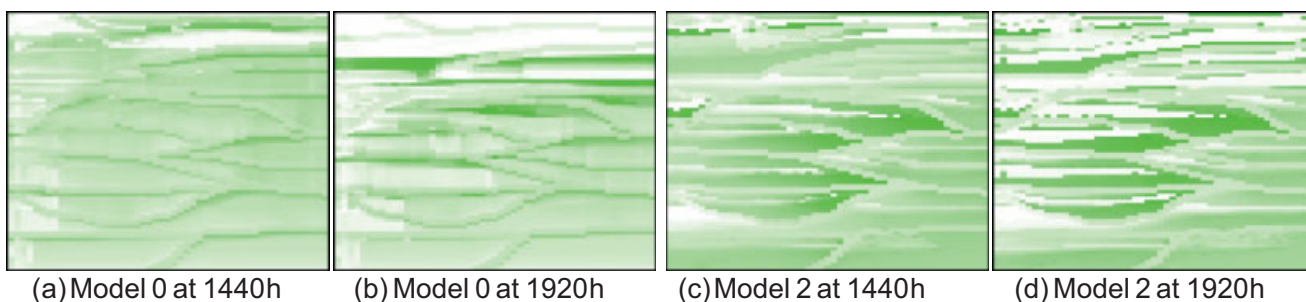
Fig. 22—Oil saturation from Models 0 and 2 after second water- and second gas-injection cycles.

(a) Model 0 at 1440h   (b) Model 0 at 1920h   (c) Model 2 at 1440h   (d) Model 2 at 1920h
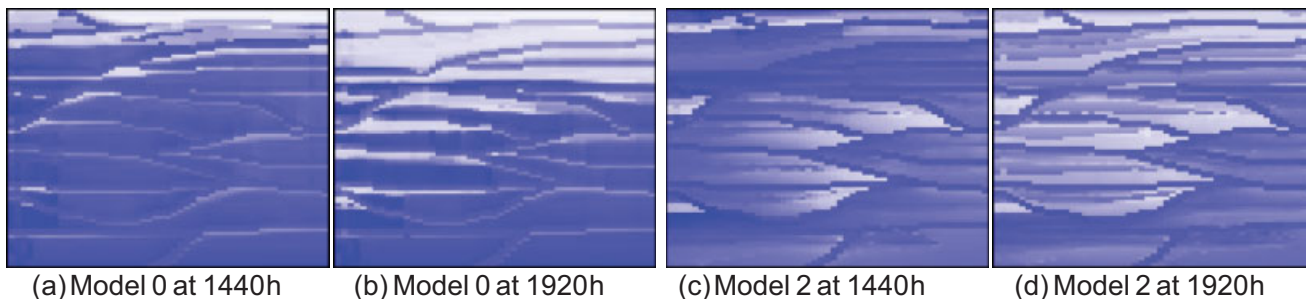
Fig. 23—Water saturation from Models 0 and 2 after second water- and second gas-injection cycles.

is selected as a base case for comparison. The production well is located centrally (Well WIA-15_A) and slightly downflank in the picture. The injection well is to the left (Well A-12_A) and is upflank to the producer. Fig. 25b shows the final saturations after water injection. The figure is an illustration of how the water sweeps in the model. WAG injection is simulated with a WAG ratio of 3:1, 3 months with water injection and 1 month with gas injection. Fig. 25c shows the final saturation after 4 years of WAG injection. The capillary pressure dependence on saturation defined by Model 1 is applied. The second capillary pressure approach (Model 2) has also been applied but was not found to have significant effect on recovery. However, setting the capillary pressures in the pressure equation to zero (Model 0) had the greatest effect on the results, although the differences were comparatively minor. These minor variations are partly the result

of the coupling of capillary pressure by means of saturation to relative permeability.

Figs. 26 and 27 illustrate various results from the water injection and WAG injection, with Models 0 and 1. Although the performance of water injection differs significantly from that of the WAG injection, the water-injection scenario is included to provide a reference case. These two figures illustrate that WAG injection can be modeled with full hysteresis applied simultaneously to all three pairs of both capillary pressure and relative permeability two-phase data. The decoupling of the capillary pressure from the pressure equation (Model 0) reduces the computation requirements by approximately 50% when compared with the inclusion of capillary pressure in the pressure equation. The main difference when not including capillary pressure in the pressure equation may be seen in the water-breakthrough time in Fig. 26c.
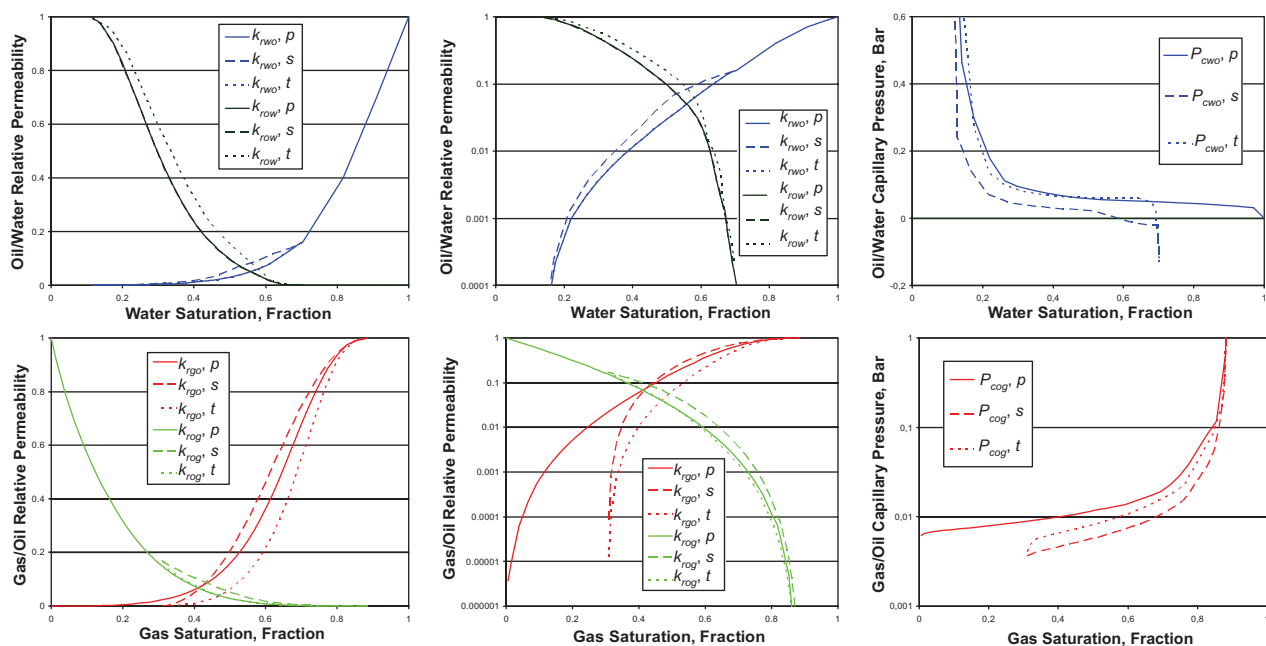

Fig. 24—One of 10 reference data sets of relative permeability and capillary pressure used in the 3D model.
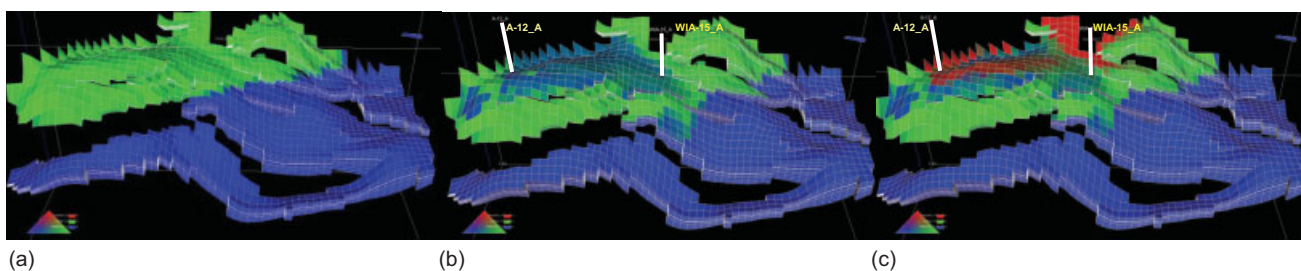
Fig. 25—Top view of initial saturation (a) and two final saturations of 3D scenarios for water- (b) and WAG- (c) injection scenarios illustrating sweep, with Model 1.
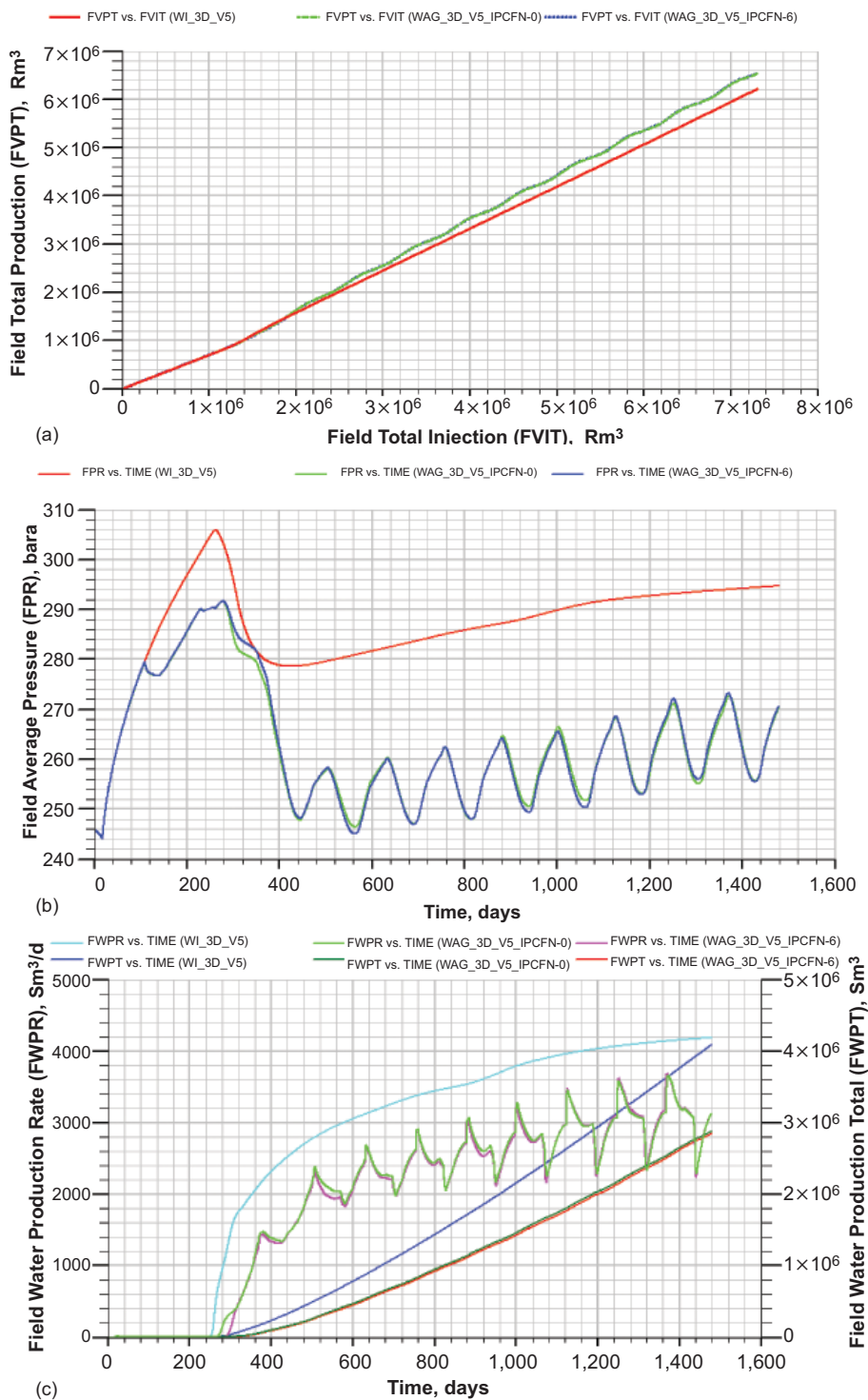

Fig. 26—(a) Field total production vs. field total injection, (b) field average pressure vs. time, and (c) field water production vs. time for water- and WAG-injection scenarios with Models 0 (WAG_3D_V5_IPCFN-0) and 1 (WAG_3D_V5_IPCFN-6).
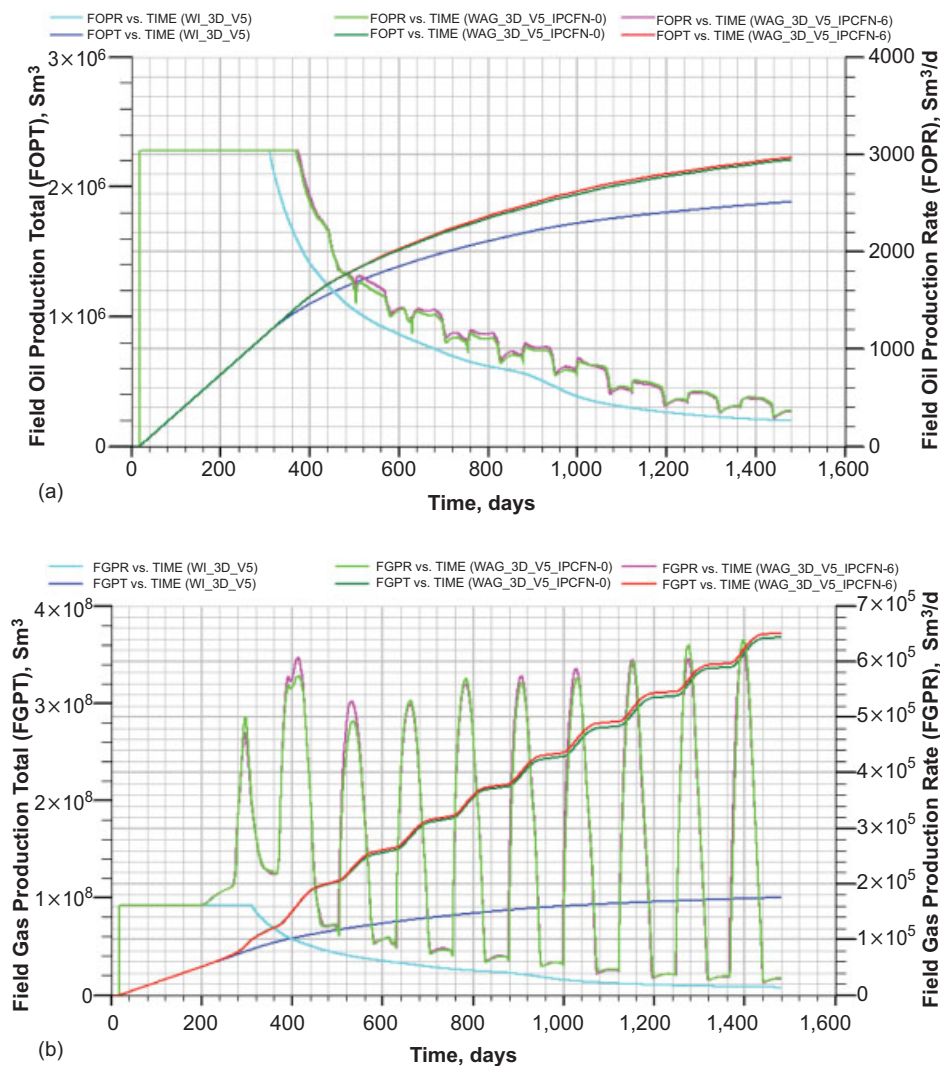
Fig. 27—Field oil (a) and gas (b) production vs. time for water- and WAG-injection scenarios, with Models 0 and 1.

Conclusions

A consistent and coupled three-phase capillary pressure and relative permeability model that incorporates hysteresis and hydrocarbon miscibility simultaneously has been implemented in a fully implicit compositional reservoir simulator.

The model incorporates varying endpoint saturations for all three phases within the three-phase space. The three-phase capillary pressure and relative permeability values are saturation-history-dependent. The model permits the capillary pressure and relative permeability data to be made dependent on one, two, or three saturations.

Test examples simulated consisting of primary, secondary, and tertiary capillary pressure and relative permeability data for typical water-wet and mixed-wet systems reveal that developing saturation profiles are strongly influenced by the capillary pressure dependence on saturation at the meter scale.

The use of three rather than the more-traditional two sets of saturation functions to model hysteresis, plus the modeling of six saturation-process directions coupled with IFT or capillary-number-weighted endpoint scaling, results in a significantly more complex model both from a simulation and an input-data-generation point of view. However, this offers a flexible and sophisticated approach to the modeling of complex reservoirs of varying properties with time and offers a variety of mechanisms for improving the match between observed and predicted recoveries.

Nomenclature

A = user-specified constant for hydrocarbon/water IFT
B = user-specified constant for hydrocarbon/water IFT

C = user-specified constant for hydrocarbon/water IFT
F = correction function for gas/oil capillary pressure
f_{ij}^{η} = scaling function for endpoint saturations and relative permeability
$f_{ij}^{P_c}$ = scaling function for capillary pressure
G = correction function for gas/water capillary pressure
H = correction function for oil/water capillary pressure
$\breve{k}_{rij}$ = input relative permeability to Phase i presence of Phase j
$\tilde{k}_{rij}$ = representative relative permeability to Phase i
$\hat{k}_{rij}$ = IFT-scaled representative relative permeability
N = number of gridblocks
n_{ij} = user-specified exponent constant for endpoint saturation and relative permeability scaling function, $i,j = g,o,w$ and $i \neq j$
P_{cij} = capillary pressure for Phases i and j
$\breve{P}_{cij}$ = input capillary pressure for Phases i and j
$\tilde{P}_{cij}$ = representative capillary pressure
$\hat{P}_{cij}$ = IFT-scaled representative capillary pressure
p = pressure
R = capillary pressure constraint residual
S = normalized saturation (input or gridblock)
$\breve{S}$ = input saturation
$\hat{S}_{irj}$ = scaled gridblock endpoint saturation
$\bar{S}$ = gridblock saturation
$\dot{S}$ = saturation derivative with respect to time
t = time
u = Darcy velocity
α_i = user-specified constant, $i = g,w$

β_i = user-specified constant, $i = g,w$
Δt = timestep size
δ_i = user-specified constant, $i=g,w$
μ = viscosity
ρ = mass density
σ_{ij} = interfacial tension between Phases i and j

Subscripts

g = gas
gro = gas endpoint in the presence of oil
grw = gas endpoint in the presence of water
imn = minimum for Phase i
imx = maximum for Phase i
o = oil
org = oil endpoint in the presence of gas
orw = oil endpoint in the presence of water
w = water
wrg = water endpoint in the presence of gas
wro = water endpoint in the presence of oil
x = x direction
y = y direction
z = z direction

Superscripts

d = decreasing
e = equivalent
h = hysteresis
i = increasing
m = scaled
max = maximum
p = primary
pr = primary reference
hr = hysteresis reference
r = reference
t = turning point or time
th = threshold
η = IFT or N_c
κ = pr or hr

Acknowledgments

References

Ahmed, T. 2006. *Reservoir Engineering Handbook*, third edition. Burlington, Massachusetts: Gulf Professional Publishing/Elsevier.

Anderson, W.G. 1986. Wettability Literature Survey—Part 2: Wettability Measurement. *J Pet Technol* **38** (11): 1246–1262. SPE-13933-PA. doi: 10.2118/13933-PA.

Anderson, W.G. 1987a. Wettability Literature Survey— Part 4: Effects of Wettability on Capillary Pressure. *J Pet Technol* **39** (10): 1283–1300. SPE-15271-PA. doi: 10.2118/15271-PA.

Anderson, W.G. 1987b. Wettability Literature Survey–Part 5: The Effects of Wettability on Relative Permeability. *J Pet Technol* **39** (11): 1453–1468. SPE-16323-PA. doi: 10.2118/16323-PA.

Aziz, K. and Settari, A. 1979. *Petroleum Reservoir Simulation*. Essex, UK: Elsevier Applied Science Publishers.

Braun, E.M. and Holland, R.F. 1995. Relative Permeability Hysteresis: Laboratory Measurements and a Conceptual Model. *SPE Res Eng* **10** (3): 222–228. SPE-28615-PA. doi: 10.2118/28615-PA.

Coats, K.H. 1980. An Equation of State Compositional Model. *J Pet Technol* **20** (5): 363–376. SPE-8284-PA. doi: 10.2118/8284-PA.

ECLIPSE Technical Description 2009.2. 2009. Abingdon, UK: Schlumberger Information Solutions.

Hinderaker, L., Utseth, R.H., Hustad, O.S., Akervoll, I., Dalland, M., Kvanvik, B.A., Austad, T., and Paulsen, J.E. 1996. RUTH—A Comprehensive Norwegian R & D Program on IOR. Paper SPE 36844 presented at the European Petroleum Conference, Milan, Italy, 22–24 October. doi: 10.2118/36844-MS.

Honarpour, M., Koederitz, L.F., and Harvey, A.H. 1986. *Relative Permeability in Reservoirs*. Boca Raton, Florida: CRC Press.

Honarpour, M.M., Huang, D.D., and Al-Hussainy, R. 1996. Simultaneous Measurements of Relative Permeability, Capillary Pressure, and Electrical Resistivity with Microwave System for Saturation Monitoring. *SPE J.* **1** (3): 283–294. SPE-30540-PA. doi: 10.2118/30540-PA.

Hustad, O.S. 2002. A Coupled Model for Three-Phase Capillary Pressure and Relative Permeability. *SPE J.* **7** (1): 59–69. SPE-74705-PA. doi: 10.2118/74705-PA.

Hustad, O.S. 2008. Method and Apparatus for Determining Capillary Pressures in a Three Phase Fluid Reservoir. US Patent Application No. 20100114506.

Hustad, O.S. and Dalen, V. 1993. An Explicit Phase-Behavior Model for Pseudocompositional Reservoir Simulation. *SPE Advanced Technology Series* **1** (1): 17–26. SPE-19806-PA. doi: 10.2118/19806-PA.

Hustad, O.S. and Holt, T. 1992. Gravity Stable Displacement of Oil by Hydrocarbon Gas after Waterflooding. Paper SPE 24116 presented at the SPE/DOE Enhanced Oil Recovery Symposium, Tulsa, 22–24 April. doi: 10.2118/24116-MS.

Hustad, O.S., Kløv, T., Lerdahl, T.R., Berge, L.I., Stensen, J.Å., and Øren, P.-E. 2002. Gas Segregation During WAG Injection and the Importance of Parameter Scaling in Three-Phase Models. Paper SPE 75138 presented at the SPE/DOE Improved Oil Recovery Symposium, Tulsa, 13–17 April. doi: 10.2118/75138-MS.

Land, C.S. 1968. Calculation of Imbibition Relative Permeability for Two- and Three-Phase Flow From Rock Properties. *SPE J.* **8** (2): 149–156; *Trans.*, AIME, **243**. SPE-1942-PA. doi: 10.2118/1942-PA.

Mattax, C.C. and Dalton, R.L. 1990. *Reservoir Simulation*. Monograph Series, SPE Richardson, Texas **13**.

Oak, M.J., Baker, L.E., and Thomas, D.C. 1990. Three-Phase Relative Permeability of Berea Sandstone. *J Pet Technol* **42** (8): 1054–1061; *Trans.*, AIME, **289**. SPE-17370-PA. doi: 10.2118/17370-PA.

Skjæveland, S.M. and Kleppe, J. ed. 1992. *Recent Advances in Improved Oil Recovery Methods for North Sea Sandstone Reservoirs*. Stavanger: SPOR Monograph Series, Norwegian Petroleum Directorate.

Skjæveland, S.M., Skauge, A., Hinderaker, L., and Sisk, C.D. eds. 1996. *RUTH, 1992–1995, A Norwegian Research Program on Improved Oil Recovery*, 183–194, 195–201. Stavanger: Norwegian Petroleum Directorate.

Spiteri, E.J., Juanes, R., Blunt, M.J., and Orr, F.M. Jr. 2008. A New Model of Trapping and Relative Permeability Hysteresis for All Wettability Characteristics. *SPE J.* **13** (3): 277–288. SPE-96448-PA. doi: 10.2118/96448-PA.

Stone, H.L. 1970. Probability Model for Estimating Three-Phase Relative Permeability. *J Pet Technol* **22** (2): 214–218; *Trans.*, AIME, **249**. SPE-2116-PA. doi: 10.2118/2116-PA.

Stone, H.L. 1973. Estimation of Three-Phase Relative Permeability and Residual Oil Data. *J. Can. Pet. Tech.* **12** (4): 53–61.

SI Metric Conversion Factors

atm $\times$ 1.013 250*	E+02	= kPa
bar $\times$ 1.0*	E+02	= kPa
cp $\times$ 1.0*	E−03	= Pa·s
(°F−32)/1.8		= °C
in. $\times$ 2.54*	E+00	= cm
md $\times$ 9.869 233	E−04	= μm^2
psi $\times$ 6.894 757	E+00	= kPa

*Conversion factor is exact.

Odd Steve Hustad is a principal researcher at Statoil's research center in Trondheim, Norway, and an adjunct professor at the Norwegian University of Science and Technology (NTNU). email: osh@statoil.com. His main research interests are within gas-based recovery methods and reservoir-simulation techniques. He holds an honors bachelor of mathematics degree in applied mathematics from the University of Waterloo, a Cand. Scient. degree (MS equivalent) in physics from the University of Trondheim, and a Doktor ingeniør degree (PhD equivalent) in petroleum engineering from the Norwegian Institute of Technology (NTH, now NTNU). He served as 1999/2000 SPE section chairperson in Trondheim. **David John Browning** is a member of the simulation development team at Schlumberger's Abingdon Technology Centre, UK. email: dbrowning@slb.com. His principal activities are the development and support of reservoir-simulation software. He holds an honors BS degree in electronic engineering from the University of Hull, MS degrees in space physics and software engineering from the Universities of Leicester and Oxford, respectively, and a PhD degree in electronic and electrical engineering from the University of Birmingham.